

Comparing 1-year GUMICS–4 simulations of the Terrestrial Magnetosphere with Cluster Measurements

G. Facskó^{1,2,3}, D. G. Sibeck², I. Honkonen⁴, J. Bór⁵, G. Farinas Perez^{2,3*},
A. Tímár¹, Y. Y. Shprits^{6,7}, L. Degener^{4†}, P. Peitso^{8‡}, E. I. Tanskanen⁸,
C. R. Anekallu⁹, J. Kalmár⁵, S. Szalai^{5,10}, Á. Kis⁵, V. Wesztergom⁵,
N. A. Aseev^{6,7}, Á. Madár^{1,11}

¹Wigner Research Centre for Physics, Budapest, Hungary

²NASA Goddard Space Flight Center, Greenbelt, Maryland, USA

³the Catholic University of America, Washington DC, USA

⁴Finnish Meteorological Institute, Helsinki, Finland

⁵Research Centre for Astronomy and Earth Sciences, Sopron, Hungary

⁶Helmholtz Centre Potsdam, GFZ German Research Centre for Geosciences, Potsdam, Germany

⁷Institute for Physics and Astronomy, University of Potsdam, Potsdam, Germany

⁸Aalto University, School of Electrical Engineering, Espoo, Finland

⁹UCL Department of Space & Climate Physics, Mullard Space Science Laboratory, Dorking, UK

¹⁰University of Miskolc, Department of Geophysics, Miskolc, Hungary

¹¹Eötvös Loránd University, Doctoral School of Physics, Budapest, Hungary

Key Points:

- The GUMICS–4 code provides realistic ion plasma moments and magnetic field in the solar wind and the outer magnetosheath.
- The code predicts realistic bow shock locations.
- An inner magnetosphere model should be added to the code to increase the accuracy of the simulation in inner magnetosphere.

*Now at University of Miami, Electrical and Computer Engineering Department, Miami, Florida, USA

†Now private individual, Hannover, Germany

‡Now at Aurora Propulsion Technologies, Espoo, Finland

Corresponding author: Gábor Facskó, facsko.gabor@wigner.hu

24 **Abstract**

25 We compare the predictions of the GUMICS-4 global magnetohydrodynamic model for
 26 the interaction of the solar wind with the Earth's magnetosphere to Cluster-3 measure-
 27 ments over for one year, from January 29, 2002, to February 2, 2003. In particular, we
 28 compare the north/south component of the magnetic field (B_z), the component of the
 29 velocity along the Sun-Earth line (V_x), and the plasma density as determined from a top
 30 hat plasma spectrometer and the spacecraft's potential. We select intervals in the so-
 31 lar wind, the magnetosheath and the magnetosphere where these instruments provided
 32 good quality data and the model correctly predicts the region in which the spacecraft
 33 is located. We determine the location of the bow shock, the magnetopause and, the neu-
 34 tral sheet from the spacecraft measurements and compare their locations to those pre-
 35 dicted by the simulation.

36 The GUMICS-4 model provides quite good results in the solar wind however its
 37 accuracy is worse in the magnetosheath. The simulation results are not realistic in the
 38 magnetosphere. The bow shock location is predicted well however the magnetopause lo-
 39 cation is less accurate. The neutral sheet positions are located quite well thanks to the
 40 special solar wind conditions.

41 **1 Introduction**

42 One of the most cost-effective way to study the interaction of the solar wind with
 43 planetary magnetospheres (or predict the conditions in near-Earth space) is modeling
 44 this complex system using a magnetohydrodynamic (MHD) code. In the past, several
 45 parallelized codes were developed, which are used and applied to forecast the cosmic en-
 46 vironment of the Earth; such as the Lyon-Fedder-Mobarry [LFM; *Lyon et al.*, 2004] code,
 47 the Grid Agnostic MHD for Extended Research Applications [GAMERA; *Zhang et al.*,
 48 2019], the Open Geospace General Circulation Model [OpenGGCM; *Raeder et al.*, 2008],
 49 the Block-Adaptive-Tree-Solarwind-Roe-Upwind-Scheme [BATS-R-US; *Powell et al.*, 1999;
 50 *Tóth et al.*, 2012]. In Europe only three global MHD codes were developed: the Grand
 51 Unified Magnetosphere–Ionosphere Coupling Simulation [GUMICS-4; *Janhunen et al.*,
 52 2012], the Computational Object Oriented Libraries for Fluid Dynamics [COOLFluiD;
 53 *Lani et al.*, 2012] and the 3D resistive magnetohydrodynamic code Gorgon [*Chittenden*
 54 *et al.*, 2004; *Ciardi et al.*, 2007]. The COOLFluiD is a general-purpose plasma simula-
 55 tion tool. The Gorgon code was developed to study high energy, collisional plasma in-

56 teractions and has been adapted to simulate planetary magnetospheres and their inter-
 57 action with the solar wind [Mejnertsen *et al.*, 2016, 2018]. Neither Gorgon nor COOLfluid
 58 have an ionospheric solver. Almost all of these codes are available at the Community Co-
 59 ordinated Modelling Center (CCMC; <http://ccmc.gsfc.nasa.gov/>) hosted by the NASA
 60 Goddard Space Flight Center (GSFC) or the Virtual Space Weather Modelling Centre
 61 (VSWMC; <http://swe.ssa.esa.int/web/guest/kul-cmpa-federated>; requires registration
 62 for the European Space Agency (ESA) Space Situational Awareness (SSA) Space Weather
 63 (SWE) portal) hosted by the KU Leuven [*Poedts et al.*, 2020]. A comparison of the sim-
 64 ulation results with spacecraft and ground-based measurements is necessary to under-
 65 stand the abilities and features of the developed tools. A statistical study using long term
 66 global MHD runs for validation of the codes seems is needed. Because providing long sim-
 67 ulations are costly and time consuming, only a few studies have been done, almost all
 68 for periods much less than a year except [*Liemohn et al.* [2018]].

69 *Guild et al.* [2008a,b] launched two months of LFM runs and compared the plasma
 70 sheet properties in the simulated tail with the statistical properties of six years Geotail
 71 magnetic field and plasma observations [*Kokubun et al.*, 1994; *Mukai et al.*, 1994]. The
 72 LFM successfully reproduced the global features of the global plasma sheet in a statis-
 73 tical sense. However, there were some differences. The sheet was too cold, too dense and
 74 the bulk flow was faster than the observed plasma sheet [*Kokubun et al.*, 1994; *Mukai*
 75 *et al.*, 1994]. The LFM overestimated the ionospheric transpolar potential. The trans-
 76 polar potential correlated with the speed of the plasma sheet flows. Equatorial maps of
 77 density, thermal pressure, thermal energy and, velocity were compared. The LFM over-
 78 estimated the plasma sheet density close to the Earth, the temperature by a factor of
 79 ~ 3 and the global average flow speed by a factor of ~ 2 . The LFM reproduced many of
 80 the climatological features of the Geotail data set. The low-resolution model underes-
 81 timated the occurrence of the fast earthward and tailward flows. Increasing the simu-
 82 lation resolution resulted in the development of fast, busty flows. These flows influenced
 83 the statistics and contributed to a better agreement between simulations and observa-
 84 tions.

85 *Zhang et al.* [2011] studied the statistics of magnetosphere-ionosphere (MI) cou-
 86 pling using *Guild et al.* [2008a]'s LFM simulation above. The polar cap potential and
 87 the field aligned currents (FAC), the downward Poynting flux and, the vorticity of the
 88 ionospheric convection were compared with observed statistical averages and the Weimer05

89 empirical model [Weimer, 2005]. The comparisons showed that the LFM model produced
 90 quite accurate average distributions of the Region 1 (R1) and Region 2 (R2) currents.
 91 The ionospheric R2 currents in the MHD simulation seemed to originate from the dia-
 92 magnetic ring current. The average LFM R1 and R2 currents were small compared with
 93 the values from the Weimer05 model. The average Cross Polar Cap Potential (CPCP)
 94 was higher in the LFM simulation than the measurements of the SuperDARN and the
 95 Weimer05 model. The average convention pattern was quite symmetric in the LFM sim-
 96 ulation against the SuperDARN measurements and the Weimer05 model. The Super-
 97 DARN measurements and the Weimer05 model had a dawn-dusk asymmetry. In the LFM
 98 model, more Poynting flux flowed into the polar region ionosphere than in the Weimer05
 99 model. It was the consequence of the larger CPCP in the LFM simulation. The larger
 100 CPCP allowed a higher electric field in the polar region. The statistical dependence of
 101 the high-latitude convection patterns on Interplanetary Magnetic Field (IMF) clock an-
 102 gle was similar to the SuperDARN measurements [Sofko *et al.*, 1995] and the Weimer05
 103 model. The average ionospheric field-aligned vorticity showed good agreement on the day-
 104 side. However, the LFM model gave a larger nightside vorticity than SuperDARN mea-
 105 surements because the Pedersen conductance on the night side ionosphere was too low.

106 *Wiltberger et al.* [2017] studied the structure of high latitude field-aligned current
 107 patterns using three resolutions of the LFM global MHD code and the Weimer05 em-
 108 pirical model [Weimer, 2005]. The studied period was a month-long and contained two
 109 high-speed streams. Generally, the patterns agreed well with results obtained from the
 110 Weimer05 computing. As the resolution of the simulations increased, the currents became
 111 more intense and narrow. The ratio of the Region 1 (R1), the Region 2 (R2) currents
 112 and, the R1/R2 ratio increased when the simulation resolution increases. However, both
 113 the R1 and R2 currents were smaller than the predictions of the Weimer05 model. This
 114 effect led to a better agreement of the LFM simulation results with the Weimer 2005 model
 115 results. The CPCP pattern became concentrated in higher latitudes because of the stronger
 116 R2 currents. The relationship of the CPCP and the R1 looked evident at a higher res-
 117 olution of the simulation. The LFM simulation could have reproduced the statistical fea-
 118 tures of the field-aligned current (FAC) patterns.

119 *Hajducek et al.* [2017] simulated the month (January,2005) using the Space Weather
 120 Modelling Framework [SWMF; Tóth *et al.*, 2005] and the OMNI solar wind data (<https://omniweb.gsfc.nasa.gov/>)
 121 as input. The simulations were compiled with and without an inner magnetosphere model

and using two different grid resolutions. The model was very good in predicting the ring currents [SYM-H; <http://wdc.kugi.kyoto-u.ac.jp/aeasy/asy.pdf>; *Iyemori*, 1990]. The K_p index (that measures the general magnetospheric convention and the auroral currents [Bartels *et al.*, 1939; Rostoker, 1972; Thomsen, 2004]) was predicted well during storms however the index was overestimated during quiet periods. The AL index (that describes the westward electrojet of the surface magnetic field introduced by *Davis and Sugiura* [1966]) was predicted reasonably well on average. However the model reached the highest negative AL value less often it was reached in the observations because the model captured the structure of the auroral zone currents poorly. The overpredicting of K_p index during quiet times might have had the same reason because that index was also sensitive to auroral zone dynamics. The SWMF usually over-predicted the CPCP. These results were not sensitive to grid resolutions, with the exception of the AL index, which reached the highest negative value more often when the grid resolution was higher. Switching off of the inner magnetosphere model had a negative effect on the accuracy of all quantities mentioned above, except the CPCP.

In this paper, the Cluster SC3 measurements are compared directly to a previously made 1-year long GUMICS-4 simulation in the solar wind, magnetosheath and the magnetosphere along the Cluster SC3 orbit saved from the simulation results and measured by the spacecraft [Facsikó *et al.*, 2016]. In this paper these parameters, namely the B_z , the north/south component of the magnetic field in GSE coordinates, the solar wind velocity GSE X component (V_x) and the solar wind density n are compared to the Cluster SC3 measurements as well as the location of the bow shock, magnetopause and the neutral sheet. These parameters are selected because B_z controls the magnetosphere, V_x is the main component of the solar wind velocity and n is the ion plasma momentum that is the easiest to calculate; furthermore more instruments could determine it (see Section 2.2). The structure of this paper is as follows. Section 2 describes the GUMICS-4 code, the 1-year simulation and the considered measurements of the Cluster space mission. Section 3 gives comparisons between the simulations and observations. Results of the comparison are discussed in Section 4. Finally, Section 5 contains the conclusions.

2 The GUMICS-4 products and Cluster measurements

Here we use two very different time series. The first type is derived from a previously 1-year run of the GUMICS-4 simulation [Facsikó *et al.*, 2016]. The second time

154 series were measured by the magnetometer, ion plasma and electric field instruments of
 155 the Cluster reference spacecraft.

156 2.1 The GUMICS–4 code

157 The GUMICS–4 has two coupled simulation domains, the magnetospheric domain
 158 outside of $3.7 R_E$ radius sphere around the Earth and a coupled ionosphere module con-
 159 taining 2D height-integrated model of ionosphere. The GUMICS–4 is not a parallel code
 160 however it has been extensively used for studying the energy propagation processes from
 161 the solar wind to the magnetosphere through the magnetopause and other features [Jan-
 162 hunen *et al.*, 2012, see the references therein]. The code has also been applied to study
 163 forced reconnection in the tail [Vörös *et al.*, 2014]. Recently, several hundred synthetic
 164 two hours duration GUMICS–4 simulation runs were made to compare the simulation
 165 results to empirical formulas [Gordeev *et al.*, 2013]. The agreement was quite good in
 166 general, but the diameter of the magnetopause in the simulation deviated significantly
 167 from observations in the tail. The GUMICS–4 simulation magnetotail was smaller than
 168 what the spacecraft observed and measured. A 1-year long simulation was made using
 169 the GUMICS–4 code [Facsikó *et al.*, 2016]. Juusola *et al.* [2014] compared the ionospheric
 170 currents, fields and the CPCP in the simulation to observations from the Super Dual Au-
 171 roral Radar Network (SuperDARN) radars [Greenwald *et al.*, 1995] and CHAMP space-
 172 craft [Reigber *et al.*, 2002] field aligned currents (FAC) measurements [Juusola *et al.*, 2007;
 173 Ritter *et al.*, 2004]. The CPCP, the FAC and other currents could not be reproduced prop-
 174 erly. The possible cause of this poor agreement could be due to low resolution in inner
 175 magnetosphere and/or the lack of an inner magnetosphere model incorporating the physics
 176 in this region. This hypothesis is supported by the result of Haiducek *et al.* [2017]. Haiducek
 177 *et al.* simulated only a month-long period using a different spatial resolution and tested
 178 the code with the inner magnetosphere model of the SWMF switched off for a special
 179 run. This run without an inner magnetosphere model made it clear that only the CPCP
 180 parameter of the simulation agreed quite well with the measurements. This fact explained
 181 why the agreement between the Cluster SC3 and the GUMICS-4 simulations was so good
 182 as described by Lakka *et al.* [2018a,b] based on the CPCP in GUMICS–4 simulations.
 183 Kallio and Facsikó [2015] determined plasma and magnetic field parameters along the
 184 lunar orbit from the Facsikó *et al.* [2016]’s global MHD simulations. The parameters dif-
 185 fered significantly in the geotail indicating a need for future studies. Facsikó *et al.* [2016]

186 determined the footprint of Cluster SC3 using the 1-year simulation and the Tsyganenko
 187 T96 empirical model [Tsyganenko, 1995]. The agreement of the footprint was better in
 188 the Northern Hemisphere. The GUMICS–4 tail was shorter in the simulations than the
 189 observations.

190 A 1-year global MHD simulation was produced with the GUMICS–4 code using
 191 the OMNI solar wind data from January 29, 2002, to February 2, 2003, as input [Facsikó
 192 *et al.*, 2016]. The creation and analysis of the simulation were based on a work package
 193 of the European Cluster Assimilation Technology (ECLAT) project (https://cordis.europa.eu/result/rcn/165813_en.html
 194 <http://www.eclat-project.eu/>). The GUMICS-4 is a serial code [Janhunen *et al.*, 2012]
 195 hence the 1-year simulation was made in 1860 independent runs. This interval covered
 196 155 Cluster SC3 orbits and each orbit lasted 57 hours. The FMI supercomputer at the
 197 time had 12 cores on each node hence the 57 hours were divided into 4.7 hours simula-
 198 tion time with one hour initialisation period. Each sub-interval used its own individual
 199 average Geocentric Solar Ecliptic (GSE) IMF magnetic field X component B_x compo-
 200 nent and dipole tilt angle. All data gaps in the solar wind were interpolated linearly. If
 201 the data gap of the input file was at the beginning (or the end) of the interval then the
 202 first (or last) good data from the input file was used to fill the gap. The initialization
 203 of each simulation run was made using constant values. These values were the first valid
 204 data of the input file repeated 60 times (60 minutes) in the input file of the sub-interval.
 205 The simulation results were saved every five minutes. Various simulation parameters, for
 206 example, the density, particle density, temperature, magnetic field, solar wind velocity
 207 (29 different quantities) were saved from the simulation results along the Cluster refer-
 208 ence spacecraft’s orbit in the GSE coordinates.

209 2.2 The Cluster SC3 measurements

210 The Cluster-II spacecraft of the European Space Agency (ESA) were launched in
 211 2000 and study the geospace [Credland *et al.*, 1997; Escoubet *et al.*, 2001]. The four space-
 212 craft form a tetrahedron in space however here we use only the measurements of the ref-
 213 erence spacecraft, Cluster SC3. The spacecraft were stabilised and their period is ~ 4 s.
 214 Hence, the intrinsic time resolution of the plasma instruments is 4 s and we use 4 s av-
 215 eraged magnetic field data. The highest resolution of the Cluster FluxGate Magnetome-
 216 ter (FGM) magnetic field instrument is 27 Hz [Balogh *et al.*, 1997, 2001]. The ion plasma
 217 data are provided by the Cluster Ion Spectrometry (CIS) Hot Ion Analyser (HIA) sub-

instrument [Reme *et al.*, 1997; Rème *et al.*, 2001]. The CIS HIA instrument is calibrated using the Waves of HIgh frequency Sounder for Probing the Electron density by Relaxation (WHISPER) wave instrument onboard Cluster [Décréau *et al.*, 2001; Trotignon *et al.*, 2010; Blagau *et al.*, 2013, 2014]. The results of these calibrations can appear as sudden non-physical jumps in the CIS HIA data. The CIS HIA had different modes to measure in the solar wind and the magnetosphere. When the instrument switched from one mode to another mode it appeared as a non-physical jumps also appear in the measurements. These features impair the accuracy of data analyses.

We protect our results from these non-physical jumps using a density determination based on different principles. We use the spacecraft potential of the Electric Field and Wave Experiment [EFW ; Gustafsson *et al.*, 1997, 2001] to determine the electron density. This quantity can be calculated using the empirical density formula

$$n_{EFW} = 200(V_{sc})^{-1.85}, \quad (1)$$

where n_{EFW} is the calculated density and V_{sc} is the Cluster EFW spacecraft potential [Trotignon *et al.*, 2010, 2011]. The EFW and the WHISPER were used for the calibration of the CIS HIA and the Plasma Electron and Current Experiment [PEACE; Johnstone *et al.*, 1997; Fazakerley *et al.*, 2010a,b]. Both instruments were still working onboard all Cluster spacecraft. Their stable operation reduced the number of data gaps, and it also made the data analysis easier.

3 Comparison of measurements to simulation

The parameters saved from the GUMICS–4 simulations and the Cluster SC3 magnetic field, solar wind velocity and, density measurements are compared in different regions, namely the solar wind, magnetosheath, and magnetosphere using cross–correlation calculation. The temporal resolution of the simulated Cluster orbit data is mostly five minutes because the results of the simulations are saved every five minutes [Facskó *et al.*, 2016]. However, the time difference between points can be more than five minutes at the boundary of the subintervals, because the length of the simulation intervals is determined in minutes. To facilitate analysis of the simulation results, all simulation data were interpolated to a one–minute resolution. This method does not provide extra information to the cross–correlation calculation. The data gaps are eliminated using linear interpolation and extrapolation when the gap is at the start or the end of the selected interval.

248 The spin resolution (4 s) of Cluster SC3 magnetic field measurements is averaged over
 249 five minutes around (± 150 s) the timestamps of the saved data. Then the averaged data
 250 were interpolated to a one-minute resolution to make easier the correlation calculations.

251 or the correlation calculation, intervals are selected carefully in the solar wind (see
 252 Section 3.1), the magnetosheath (see Section 3.2), the dayside and the night side mag-
 253 netosphere (see Section 3.3). In these intervals, the parameters did not vary a lot and
 254 we require neither Cluster nor the virtual probe to cross any boundaries. To compare
 255 the B_z magnetic field, V_x solar wind speed and the n_{CIS} and the n_{EFW} curves we cross
 256 correlate selected intervals. We carefully examine such cases and remove intervals which
 257 are too short for the ± 60 minutes correlation calculation (shorter than four hours) and
 258 large data gaps from the correlation calculation. Those intervals are also neglected where
 259 the plasma instrument has a calibration error or a change in its recording mode as it moves
 260 from the magnetosphere to solar wind (for example). The electron density is also cal-
 261 culated using Equation 1 and correlated. We want to avoid the calibration errors and
 262 sudden non-physical jumps mentioned previously. The correlation results for the den-
 263 sity derived from the electric field potential results do not differ significantly from those
 264 for the top hat plasma instrument, however the n_{EFW} does not have any mode change
 265 and it is applicable in the magnetosphere too (against the CIS HIA instrument).

266 3.1 Solar wind

267 We use OMNI IMF and solar wind velocity, density, and temperature data as in-
 268 put to the simulation. There is a reason why we compare parameters in the solar wind
 269 region in the simulation and the measurements. The IMF X component cannot be given
 270 to the GUMICS-4 as input [Janhunen *et al.*, 2012; Fazekas *et al.*, 2016]. However, the
 271 magnetic field of the solar wind has an X component in the simulations. Additionally,
 272 the solar wind structure might change from the simulation domain boundary at $+32 R_E$
 273 to the sub-solar point of the terrestrial bow shock where all OMNI data is shifted. Al-
 274 most the same solar wind time intervals are used as in Table 1 of Fazekas *et al.* [2016].
 275 The number of these intervals is small because Cluster fleet instruments were calibrated
 276 in 2002, just after launch (Table 1). Hence we do not have a satisfactory ion plasma data
 277 coverage for this year. Additionally, to improve the accuracy of the correlation calcu-
 278 lation (see below) we delete the intervals that were too short (shorter than five hours)
 279 or the CIS HIA instrument changed its mode. The Cluster fleet is located in the solar

wind only from December to May and only for a couple of hours during each orbit near apogee. We double-check whether the Cluster SC3 stays in the solar wind in both the simulation and reality. We also check the omnidirectional CIS HIA ion spectra on the Cluster Science Archive (CSA; <https://www.cosmos.esa.int/web/csa/csds-quicklook-plots>). The spectra must contain one narrow band in the solar wind region. Hence 17 intervals are left in the solar wind to study (Figure 1).

The selected intervals occur for quiet solar wind conditions (Figure 2). The GUMICS-4 simulation results have five minutes resolution and the Cluster SC3 measurements have one minute resolution (Figure 3). The measurements vary significantly. In spite of the quiet conditions the solar wind density often changes and deviates from the simulation. Figure 4c shows that both densities deviate significantly. The CIS HIA density deviation is larger as expected given the complexity and the large number of working modes of the CIS instrument. The magnetic field and the solar wind velocity fit better. Figure 5a shows that the correlation of the magnetic fields is very good; furthermore on Figure 5c, 5e, 5g the correlation of the solar wind velocity and density is excellent (Table 1). The time shift on Figure 5b, Figure 5d, Figure 5f is about five minutes for the magnetic field and the CIS data. On Figure 5h for the EFW data the time shift is less stable. It is not as well determined as in case of the other parameters.

3.2 Magnetosheath

The Cluster SC3 spent only a little time in the solar wind from December, 2002 to May, 2003. However, the spacecraft enters the magnetosheath each orbit (Figure 6). We selected intervals when the value of the magnetic field is around 25 nT. The field should be fluctuating because of the turbulent deflected flow of the shocked solar wind the temperature should be greater than that in the solar wind. The velocity should decrease to values ranging from 100-300 km/s. The density of the plasma should increase and reached values of $10\text{-}20 \text{ cm}^{-3}$. The narrow band on the omnidirectional CIS HIA ion spectra from the CSA (<https://www.cosmos.esa.int/web/csa/csds-quicklook-plots>) widens from the solar wind to the magnetosheath. 15–30 minutes from each bow shock crossing we considered the Cluster SC3 to have entered into the magnetosheath. At the inner magnetopause boundary of the magnetopause the flow speed and the density drop. The magnetic field strength increases and the magnetic field becomes less turbulent than in the magnetosheath. The wide band on the the omnidirectional CIS HIA ion spectra disap-

312 pears. 15–30 minutes before the appearance of these indicators of the magnetopause crossing
 313 our intervals end. All intervals contain large data gaps, non-physical jump in instru-
 314 ment modes or lasting less than four hour are removed. Hence 74 intervals considered
 315 in our final selection (Table 2).

316 All intervals have quiet upstream (or input) solar wind conditions (Figure 7). In-
 317 spite of our selected magnetic field and plasma parameters and the calculated empiri-
 318 cal density indicate that they vary significantly stronger than in the solar wind intervals
 319 (Figure 8). The deviation between the simulated and the observed data is also larger in
 320 this region. The scatter plots of the magnetic field, plasma flow speed and the densities
 321 show that these parameters agree well, but with greater variation than the scatter plots
 322 for the solar wind (Figure 9a, 9b, 9c). The correlation of the simulated and the observed
 323 data is good for the magnetic field (Figure 10a), very good for the ion plasma moments
 324 and the calculated density (Figure 10c, 10e, 10g). The timeshift of the magnetic field
 325 is within five minutes mostly (Figure 10b) however the timeshift of the ion plasma mo-
 326 ments is scattered (Figure 10d, 10f). The timeshift of the calculated EFW density seems
 327 to be more stable (Figure 10h). Generally, the GUMICS–4 is less accurate in the mag-
 328 netosheath than in the solar wind. The modelled magnetic field is closer to the obser-
 329 vations than the modelled plasma parameters are. The calculated empirical EFW den-
 330 sity (n_{EFW}) fits better than the CIS HIA density (n_{CIS}).

331 3.3 Magnetosphere

332 To select intervals in the magnetosphere we looked for the CIS HIA omnidirectional
 333 ion flux spectrum. Where the band of the hot magnetosheath ion population (dis)appeared,
 334 the magnetosphere started/finished. The plasma density decreases toward zero, the mag-
 335 netic field strength is large. We left 15–30 min after/before the magnetopause transition
 336 to identify magnetosphere intervals. This way we found 132 intervals in the magneto-
 337 sphere (Table 3) using Cluster SC3 measurements. Cluster SC3 spends considerable time
 338 in the magnetosphere (Figure 11).

339 Here we show neither any correlation calculation nor comparison plot. In the mag-
 340 netosphere, the GUMICS–4 does not work well. Neither the magnetic field nor the plasma
 341 moments nor the N_{EFW} fit well. The solar wind velocity does not reach zero in the sim-
 342 ulation. Instead, the solar wind enters the night side magnetosphere. The solar wind CIS

343 HIA ion plasma density and the calculated density from spacecraft potential increase closer
 344 to the Earth (plasmasphere). The GUMICS–4 density is low there. We calculated the
 345 dipole field in GSE using Tsyganenko Geotool box [Tsyganenko, 1995] and subtracted
 346 from both the observed and the simulated magnetic field B_z data. The correlation of these
 347 corrected magnetic field measurements and simulations is very low too.

348 **3.4 Bow shock, magnetopause, neutral sheet**

349 77 intervals are selected when Cluster SC3 crossed the terrestrial bow shock once
 350 or multiple times (Table 6). When the spacecraft crosses the bow shock inbound the mag-
 351 nitude of the magnetic field and the solar wind density increases by a factor of 4–5 times
 352 (from 5 nT or 5 cm^{-3} , respectively), the solar wind speed drops from 400–600 km/s to
 353 100–300 km/s; furthermore the narrow band on the omnidirectional Cluster CIS HIA ion
 354 spectra widens. Both the Cluster measurements and the GUMICS–4 simulations have
 355 5-min resolution and are interpolated to 1-min resolution. All bow shock transitions of
 356 the virtual spacecraft are slower and smoother. Additionally, the multiple bow shock trans-
 357 itions are not visible in the GUMICS simulations. The code reacts slowly to such sud-
 358 den changes. The magnetic signatures fit better than the calculated plasma moments.
 359 The jump of the ion plasma parameters and the derived Cluster EFW density of the sim-
 360 ulations are shifted to the measurements. Generally, the density and the velocity of the
 361 simulations seem to be less accurate than the magnetic field of the simulations.

362 54 intervals are selected around magnetopause crossings (Table 7). When the space-
 363 craft crosses the magnetopause inbound the magnitude of the magnetic field increases,
 364 the solar wind speed drops from 100–300 km/s to zero, the plasma density becomes zero;
 365 furthermore the wide band on the omnidirectional Cluster CIS HIA ion spectra disap-
 366 pears. The location of the magnetopause is well determined by the Cluster SC3 mea-
 367 surements. However, it is very difficult to identify the magnetopause crossings in the sim-
 368 ulation data. The magnetopause crossings very often cannot be seen in the simulations.
 369 Or when the magnetopause crossings are identified in both simulations and spacecraft
 370 measurements the events are shifted. The accuracy of the model is lower for the dayside
 371 magnetopause locations.

372 Nine intervals are chosen around Cluster SC3 neutral sheet crossings (Figure 12;
 373 Table 8). The neutral sheet locations are determined using the results of the Boundary

374 Layer Identification Code (BLIC) Project [Facskó *et al.*, in preparation]. The BLIC code
 375 determines the neutral sheet crossing Cluster FGM magnetic field measurements using
 376 *Wang and Xu* [1994]’s method. When the solar wind speed is almost zero; furthermore
 377 the CIS HIA density and the EFW calculated density are almost zero too; finally the GSE
 378 Z component of the magnetic field changes is a sign of the code indicated neutral sheet
 379 crossing (Figure 19; red and blue curves). The neutral sheet crossings are visible very
 380 well in the GUMICS simulations (Figure 19; black curves). For five events (from nine
 381 Cluster SC3 crossings) the GUMICS–4 also provides similar smoothed parameters and
 382 change of sign of the B_z component. This is a outstanding result because the tail in the
 383 GUMICS–4 simulations is significantly smaller than the observed reality [*Gordeev et al.*,
 384 2013; *Facskó et al.*, 2016]; furthermore the solar wind enters the tail in MHD simulations
 385 generally [*Kallio and Facskó*, 2015].

386 4 Discussion

387 The agreement of B_z , V_x and n_{EFW} in the solar wind with the similar GUMICS
 388 simulation predictions is very good (Figure 4a, 4b, 4c, blue). The agreement of n_{CIS} is
 389 worse (Figure 4c, red). It was expected because the n_{EFW} depends on the spacecraft
 390 potential provided by the EFW instrument. However, the CIS instrument has many modes
 391 for measuring the plasma parameters and it needs periodic calibration too. The corre-
 392 lation of the solar wind V_x , n_{CIS} and n_{EFW} with the similar GUMICS simulation pa-
 393 rameters is greater than 0.9 (Figure 5c, 5e, 5g). The correlation of the B_z is also greater
 394 than 0.8 (Figure 5a). The upstream boundary of the GUMICS–4 code lies at $32 R_E$ [*Jan-*
 395 *hunen et al.*, 2012], the nose of the terrestrial bow shock is at about $20 R_E$. If the so-
 396 lar wind speed is 400 km/s, then this spatial distance means less than a 5 minutes de-
 397 lay, so it should not be visible in the time delays from the cross correlations. 80% of the
 398 intervals support this theory but 20 % do not. In these cases, the one-minute resolution
 399 B_z , n_{CIS} or the n_{EFW} parameters have a sudden jump or variation that the simulation
 400 cannot follow, or the resolution of the simulation output (5 minutes) is too small to see
 401 these variations. Therefore, the correlation calculation is not accurate in these cases. Pre-
 402 viously the OMNI data was compared to the Cluster data and the Cluster measurements
 403 were compared to the GUMICS–4 [*Facskó et al.*, 2016]. The comparison suggests that
 404 the GUMICS–4 results should be similar for the OMNI data. Furthermore, we calcu-
 405 late correlation functions in the solar wind, where there is no significant perturbation

406 of the input parameters in the simulation box. Therefore, we get the expected result af-
 407 ter comparing the two different correlation calculations.

408 In the magnetosheath we get worse agreement with the GUMICS simulation data
 409 (Figure 9a, 9b, 9c). While the parameters are correlated, the scatter is greater. The gen-
 410 eral reason for this larger uncertainty seems to be that the magnetosheath is turbulent.
 411 This phenomenon explains the higher variations of the B_z magnetic field on Figure 9a.
 412 The solar wind V_x , n_{CIS} and n_{EFW} agree better than the magnetic field component (Fig-
 413 ure 9b, 9c). Here there is no deviation between the densities derived in different ways
 414 (n_{CIS} and n_{EFW}) on Figure 9c. Figure 10 seems to contradict these statements above.
 415 The larger uncertainty of the B_z is visible in Figure 10a. However, that correlation is
 416 still good in Figure 10b. The other parameters have larger (> 0.9) correlation in Fig-
 417 ure 10c, 10e, 10g. However, the time shifts in Figure 10d, 10f, 10h seem to be worse. Here
 418 the time shifts are worse because the shape of the time series in the magnetosheath looks
 419 very smooth and similar hence there are not enough points to get a sharp and large max-
 420 imum correlation as the function of timeshift. The difference between the minimum and
 421 the maximum of the correlation is small comparing with the uncertainty of the calcu-
 422 lation. The maximum, the timeshift could be anywhere and the shape of the correlation
 423 vs. timeshift function is often neither symmetric nor has only one local maximum. Hence,
 424 the correlation calculation provides larger time shifts for the ion plasma parameters and
 425 the n_{EFW} .

426 In the magnetosphere the GUMICS–4 does not work well. GUMICS–4 uses a tilted
 427 dipole to describe the terrestrial magnetic field [Janhunen *et al.*, 2012]. After removing
 428 the magnetic dipole from the magnetic field measurements of the Cluster SC3 and the
 429 simulation we get very low correlations and unacceptable time shifts (not shown). The
 430 tilted dipole is an insufficient description of the inner magnetospheric magnetic field. The
 431 plasma moments and the n_{EFW} do not fit either. The single fluid, ideal MHD does not
 432 describe the inner magnetosphere well therefore V_x and n in the simulations do not agree
 433 with V_x , n_{CIS} and the n_{EFW} measured by the Cluster SC3. Within the $3.7 R_E$ domain
 434 ring current physics must be added, as it has been in other global MHD codes [for ex-
 435 ample Tóth *et al.*, 2012]. This can explain the limited accuracy of the cross polar cap
 436 potential (CPCP) and geomagnetic indices of the GUMICS simulations [Juusola *et al.*,
 437 2014]. The CPCP GUMICS agrees well with spacecraft measurements therefore this quan-
 438 tity could be used for simulation studies [Lakka *et al.*, 2018a]. Haiducek *et al.* [2017] also

439 compared geomagnetic indices and the CPCP. The Space Weather Modelling Framework
 440 (SWMF) was tested. When the inner magnetosphere model was switched off in the sim-
 441 ulation only the comparison of the simulated and observed CPCP was good. Therefore,
 442 the reason of the discrepancy of the geomagnetic indices in the GUMICS simulations must
 443 be the missing inner magnetosphere model.

444 The reason of why simulation results and measurements disagree could be the code
 445 or the bad input parameters. During the 1-year run the distributions of the OMNI so-
 446 lar wind magnetic field B_x , B_y , B_z components; solar wind velocity V_x , V_y , V_z com-
 447 ponents and the solar wind P dynamic pressure are calculated from January 29, 2002 to
 448 February 2, 2003 in GSE reference frame. These distributions of the OMNI solar wind
 449 magnetic field B_x , B_y , B_z components were overplotted by red in Figure 13a, 13d, 13g, 13j
 450 and Figure 16a, 16d, 16g, 16j; Figure 13b, 13e, 13h, 13k and Figure 16b, 16e, 16h, 16k;
 451 furthermore Figure 13c, 13f, 13i, 13l and Figure 16c, 16f, 16i, 16l. These distributions
 452 of the OMNI solar wind velocity V_x , V_y , V_z components were overplotted by red in Fig-
 453 ure 14a, 14d, 14g, 14j and Figure 17a, 17d, 17g, 17j; Figure 14b, 14e, 14h, 14k and Fig-
 454 ure 17b, 17e, 17h, 17k; furthermore Figure 14c, 14f, 14i, 14l and Figure 17c, 17f, 17i, 17l.
 455 These distributions of the P solar wind pressure calculated from the OMNI solar wind
 456 parameters were overplotted by red in Figure 15a, 15b, 15c, 15d and Figure 18a, 18b, 18c, 18d.
 457 The intervals when the GUMICS–4 simulations and the Cluster SC3 measurements dis-
 458 agreed are collected for intervals in the solar wind (Table 4) and the magnetosheath (Ta-
 459 ble 5). The definition of disagreement of the simulations and measurements is quite ar-
 460bitrary. When the two curves deviate or the correlation function is not symmetric we con-
 461 sidered the simulations and the measurements disagreeing. The correlations correlation
 462 coeffitiens are also high in this cases however the time shift is large (~ 60 min). The av-
 463 eraged shifted OMNI parameters of the poorly agreeing intervals from the Tables 4 and 5
 464 are saved. The distributions of the OMNI parameters belonging to the bad simulation
 465 results are calculated for the solar wind region (Figure 13, 14 and 15) and in the mag-
 466 netosheath (Figure 16, 17 and 18).

- 467 1. In the solar wind the distributions of the OMNI B_x , B_y and B_z can be compared
 468 in Figure 13a, 13d, 13g, 13j; Figure 13b, 13e, 13h, 13k; furthermore in Figure 13c, 13f, 13i, 13l.
 469 (a) When the B_z disagrees in simulations and measurements in Figure 13a, 13b, 13c
 470 the black and red distributions of the OMNI B_x , B_y and B_z are not similar.

471 The reason of these strange spikes is that there is only one poorly correlated
 472 interval for the B_z in the solar wind according to Table 4.

- 473 (b) When the V_x disagrees in simulations and measurements in Figure 13d, 13e, 13f
 474 the black and red distributions of the OMNI B_x , B_y and B_z are similar. The
 475 distributions do not agree perfectly because in Table 4 the number of the poorly
 476 correlated intervals is only six for the V_x component.
- 477 (c) When the n_{CIS} disagrees in simulations and measurements in Figure 13g, 13h, 13i
 478 the black and red distributions of the OMNI B_x , B_y and B_z are similar. The
 479 distributions do not agree perfectly because in Table 4 the number of the poorly
 480 correlated intervals is only 12 for the n_{CIS} .
- 481 (d) When the n_{EFW} disagrees in Figure 13j, 13k, 13l the black and red distribu-
 482 tions of the OMNI B_x , B_y and B_z are similar. The distributions do not agree
 483 perfectly because in Table 4 the number of the poorly correlated intervals is only
 484 nine for n_{EFW} .

485 The values of the OMNI B_x , B_y , and B_z are not peculiar in the solar wind.

- 486 2. In the solar wind the distributions of the OMNI V_x , V_y and V_z can be compared
 487 in Figure 14a, 14d, 14g, 14j; Figure 14b, 14e, 14h, 14k; furthermore in Figure 14c, 14f, 14i, 14l.
- 488 (a) When the B_z disagrees in Figure 14a, 14b, 14c the black and red distributions
 489 of the OMNI V_x , V_y and V_z are not similar. The reason of these strange spikes
 490 is that there is only one poorly correlated interval for the B_z in the solar wind
 491 according to Table 4.
- 492 (b) When the V_x disagrees in simulations and measurements in Figure 14d, 14e, 14f
 493 the black and red distributions of the OMNI V_x , V_y and V_z are similar. The dis-
 494 tributions do not agree perfectly because in Table 4 the number of the poorly
 495 correlated intervals is only six for the V_x component.
- 496 (c) When the n_{CIS} disagrees in Figure 14g, 14h, 14i the black and red distributions
 497 of the OMNI V_x , V_y and V_z are similar. The distributions do not agree perfectly
 498 because in Table 4 the number of the poorly correlated intervals is only 12 for
 499 the n_{CIS} .
- 500 (d) When the n_{EFW} disagrees in simulations and measurements in Figure 14j, 14k, 14l
 501 the black and red distributions of the OMNI V_x , V_y and V_z are similar. The dis-

502 tributions do not agree perfectly because in Table 4 the number of the poorly
 503 correlated intervals is only nine for the n_{EFW} .

504 The values of the OMNI V_x , V_y , and V_z are not peculiar in the solar wind.

505 3. In the solar wind the distributions of the solar wind P calculated from OMNI pa-
 506 rameters can be compared in Figure 15a, 15b, 15c, 15d.

- 507 (a) When the B_z disagrees in Figure 15a the black and red distributions of the OMNI
 508 P are not similar. The reason of these strange spike is that there is only one
 509 poorly correlated interval for the B_z in the solar wind according to Table 4.
- 510 (b) When the V_x disagrees in simulations and measurements in Figure 15b the black
 511 and red distributions of the OMNI P are similar. The distributions do not agree
 512 perfectly because in Table 4 the number of the poorly correlated intervals is only
 513 six V_x component.
- 514 (c) When the n_{CIS} disagrees in simulations and measurements in Figure 15c the
 515 black and red distributions of the OMNI P are similar. The distributions do
 516 not agree perfectly because in Table 4 the number of the poorly correlated in-
 517 tervals is only 12 for the n_{CIS} .
- 518 (d) When the n_{EFW} disagrees in simulations and measurements in Figure 15d the
 519 black and red distributions of the OMNI P are similar. The distributions do
 520 not agree perfectly because in Table 4 the number of the poorly correlated in-
 521 tervals is only nine for the n_{EFW} .

522 The values of the OMNI P are not peculiar in the solar wind.

523 4. In the magnetosheath the distributions of the OMNI B_x , B_y and B_z can be com-
 524 pared in Figure 16a, 16d, 16g, 16j; Figure 16b, 16e, 16h, 16k; furthermore in Fig-
 525 ure 16c, 16f, 16i, 16l.

- 526 (a) When the B_z disagrees in simulations and measurements in Figure 16a, 16b, 16c
 527 the black and red distributions of the OMNI B_x , B_y and B_z are similar.
- 528 (b) When the V_x disagrees in simulations and measurements in Figure 16d, 16e, 16f
 529 the black and red distributions of the OMNI B_x , B_y and B_z are similar.
- 530 (c) When the n_{CIS} disagrees in simulations and measurements in Figure 16g, 16h, 16i
 531 the black and red distributions of the OMNI B_x , B_y and B_z are similar.
- 532 (d) When the n_{EFW} disagrees in Figure 16j, 16k, 16l the black and red distribu-
 533 tions of the OMNI B_x , B_y and B_z are similar.

534 The distributions agree quite well because in Table 5 the number of the poorly
 535 correlated intervals 18, 50, 33 and 30 for the B_z , the V_x , the n_{CIS} and n_{CIS} com-
 536 ponents, respectively. The number of cases is higher and the values of the OMNI
 537 B_x , B_y and B_z are not peculiar in the magnetosheath.

538 5. In the magnetosheath the distributions of the OMNI V_x , V_y and V_z can be com-
 539 compared in Figure 17a, 17d, 17g, 17j; Figure 17b, 17e, 17h, 17k; furthermore in Fig-
 540 ure 17c, 17f, 17i, 17l.

- 541 (a) When the B_z disagrees in Figure 17a, 17b, 17c the black and red distributions
 542 of the OMNI V_x , V_y and V_z are similar.
- 543 (b) When the V_x disagrees in simulations and measurements in Figure 17d, 17e, 17f
 544 the black and red distributions of the OMNI V_x , V_y and V_z are similar.
- 545 (c) When the n_{CIS} disagrees in Figure 17g, 17h, 17i the black and red distributions
 546 of the OMNI V_x , V_y and V_z are similar.
- 547 (d) When the n_{EFW} disagrees in simulations and measurements in Figure 17j, 17k, 17l
 548 the black and red distributions of the OMNI V_x , V_y and V_z are similar.

549 The distributions agree quite well because in Table 5 the number of the poorly
 550 correlated intervals 18, 50, 33 and 30 for the B_z , the V_x , the n_{CIS} and n_{CIS} com-
 551 ponents, respectively. The number of cases is higher and the values of the OMNI
 552 V_x , V_y and V_z are not peculiar in the magnetosheath.

553 6. In the magnetosheath the distributions of the solar wind P calculated from OMNI
 554 parameters can be compared in Figure 18a, 18b, 18c, 18d.

- 555 (a) When the B_z disagrees in Figure 18a the black and red distributions of the OMNI
 556 P are similar.
- 557 (b) When the V_x disagrees in simulations and measurements in Figure 18b the black
 558 and red distributions of the OMNI P are similar.
- 559 (c) When the n_{CIS} disagrees in simulations and measurements in Figure 18c the
 560 black and red distributions of the OMNI P are similar.
- 561 (d) When the n_{EFW} disagrees in simulations and measurements in Figure 18d the
 562 black and red distributions of the OMNI P are similar.

563 The distributions agree quite well because in Table 5 the number of the poorly
 564 correlated intervals 18, 50, 33 and 30 for the B_z , the V_x , the n_{CIS} and n_{CIS} com-

565 ponents, respectively. The number of cases is higher and the values of the OMNI
 566 P are not peculiar in the magnetosheath.

567 The inaccuracy of the GUMICS-4 simulations does not depend on the OMNI parame-
 568 ters in the solar wind and magnetosheath regions. The same study does not need to be
 569 done for the magnetosphere because the deviation of the measurements and the simu-
 570 lations are so large that it cannot be caused by the wrong OMNI solar wind parameters.

571 The bow shock positions agree in the GUMICS simulations and the Cluster SC3
 572 measurements. However, the magnetopause locations do not fit well as the bow shock
 573 in simulations and observations. In simulations the location of the magnetopause is de-
 574 termined from peaks in currents density, particle density gradient, or changes in flow ve-
 575 locity [Siscoe *et al.*, 2001; García and Hughes, 2007; Gordeev *et al.*, 2013, see references
 576 therein]. In this paper the previously saved simulation parameters along the virtual Clus-
 577 ter SC3 orbit are analysed. The J_y current density component cannot be calculated from
 578 only the Cluster SC3 measurements. Therefore, the above mentioned methods cannot
 579 be applied. This discrepancy of the magnetopause location agrees with the results of Gordeev
 580 *et al.* [2013] and Facskó *et al.* [2016]. Gordeev *et al.* [2013] compared synthetic GUMICS
 581 runs with an empirical formula for the magnetopause locations. Facskó *et al.* [2016] used
 582 OMNI solar wind data as input and got the same result as Gordeev *et al.* [2013] and this
 583 paper. The neutral sheets are visible in both simulations and observations (Figure 19, Ta-
 584 ble 8). This experience is exceptional because the night side magnetosphere of the GUMICS-4
 585 simulations is small and twisted [Gordeev *et al.*, 2013; Facskó *et al.*, 2016]. However, in
 586 these cases the IMF has no large B_y component. From Facskó *et al.* [2016] we know that
 587 the GUMICS has normal long tail (or night side magnetosphere) if the B_y is small.

588 5 Summary and conclusions

589 Based on the previously created 1-year long GUMICS-4 run global MHD simu-
 590 lation results are compared with Cluster SC3 magnetic field, solar wind velocity and den-
 591 sity measurements along the spacecraft orbit. Intervals are selected when the Cluster SC3
 592 and the virtual space probe are situated in the solar wind, magnetosheath and the mag-
 593 netosphere and their correlation are calculated. Bow shock, magnetopause and neutral
 594 sheet crossings are selected and their visibility and relative position are compared. We
 595 achieved the following results:

- 596 1. In the solar wind the correlation coefficient of the B_z , the V_x , the n_{EFW} and the
 597 n_{CIS} are larger than 0.8, 0.9, 0.9 and 0.9, respectively. The agreement of the B_z ,
 598 the V_x and the n_{EFW} is very good, furthermore the agreement of the n_{CIS} is also
 599 good.
- 600 2. In the magnetosheath the correlation coefficient of the B_z , the V_x , the n_{EFW} and
 601 the n_{CIS} are larger than 0.6, 0.9, 0.9 and 0.9, respectively. The agreement of the
 602 magnetic field component, the ion plasma moments and the calculated empirical
 603 density is a bit worse than in the solar wind. The V_x , the n_{EFW} and the n_{CIS} fits
 604 better than the B_z component in the magnetosheath. Their agreement is still good.
 605 The reason of the deviation is the turbulent behavior of the slowed down and ther-
 606 malised turbulent solar wind.
- 607 3. In neither the dayside nor the nightside magnetosphere can the GUMICS-4 pro-
 608 vide realistic results. The simulation outputs and the spacecraft measurement dis-
 609 agree in this region. The reason of this deviation must be the missing coupled in-
 610 inner magnetosphere model. The applied tilted dipole approach is not satisfactory
 611 in the magnetosphere at all.
- 612 4. Disagreement between GUMICS-4 and observations does not seem to be due to
 613 upstream solar wind.
- 614 5. The position of the bow shock and the neutral sheet agrees well in the simulations
 615 and the Cluster SC3 magnetic field, ion plasma moments and derived electron den-
 616 sity measurements in this study. The position of the magnetopause does not fit
 617 that well.

618 The GUMICS-4 has scientific and strategic importance for the European Space Weather
 619 and Scientific community. This code developed in the Finnish Meteorological Institute
 620 is the most developed and tested, widely used tool for modelling the cosmic environment
 621 of the Earth in the Europe. An inner magnetosphere model should be two way coupled
 622 to the existing configuration of the simulation tool to improve the accuracy of the sim-
 623 ulations.

624 Acknowledgments

625 The OMNI data were obtained from the GSFC/SPDF OMNIWeb interface at <http://omniweb.gsfc.nasa.gov>.
 626 The authors thank the FGM Team (PI: Chris Carr), the CIS Team (PI: Iannis Dandouras),
 627 the WHISPER Team (PI: Jean-Louis Rauch), the EFW Team (PI: Mats Andre) and the

628 Cluster Science Archive for providing FGM magnetic field, CIS HIA ion plasma and WHIS-
 629 PER electron density measurements. Data analysis was partly done with the QSAS sci-
 630 ence analysis system provided by the United Kingdom Cluster Science Centre (Impe-
 631 rial College London and Queen Mary, University of London) supported by the Science
 632 and Technology Facilities Council (STFC). Eija Tanskanen acknowledges financial sup-
 633 port from the Academy of Finland for the ReSoLVE Centre of Excellence (project No. 272157).
 634 Gábor Facskó thanks Anna-Mária Vígh for improving the English of the paper. The au-
 635 thors thank Pekka Janhunen for developing the GUMICS-4 code; furthermore Minna
 636 Palmroth and Zoltán Vörös for the useful discussions. The work of Gábor Facskó was
 637 supported by mission science funding for the Van Allen Probes mission, the American
 638 Geophysical Union and the HAS Research Centre for Astronomy and Earth Sciences,
 639 Sopron, Hungary. For further use of the year run data, request the authors or use the
 640 archive of the Community Coordinated Modelling Center (https://ccmc.gsfc.nasa.gov/publications/posted_runs/Facskó et al., 2018).

641

642 References

- 643 Balogh, A., M. W. Dunlop, S. W. H. Cowley, D. J. Southwood, J. G. Thomlinson,
 644 K. H. Glassmeier, G. Musmann, H. Luhr, S. Buchert, M. H. Acuna, D. H. Fair-
 645 field, J. A. Slavin, W. Riedler, K. Schwingenschuh, and M. G. Kivelson (1997),
 646 The Cluster Magnetic Field Investigation, *Space Science Reviews*, **79**, 65–91, doi:
 647 [10.1023/A:1004970907748](https://doi.org/10.1023/A:1004970907748).
- 648 Balogh, A., C. M. Carr, M. H. Acuña, M. W. Dunlop, T. J. Beek, P. Brown,
 649 K. Fornacon, E. Georgescu, K. Glassmeier, J. Harris, G. Musmann, T. Oddy, and
 650 K. Schwingenschuh (2001), The Cluster Magnetic Field Investigation: overview of
 651 in-flight performance and initial results, *Annales Geophysicae*, **19**, 1207–1217.
- 652 Bartels, J., N. H. Heck, and H. F. Johnston (1939), The three-hour-range index mea-
 653 suring geomagnetic activity, *Terrestrial Magnetism and Atmospheric Electricity*
 654 (*Journal of Geophysical Research*), **44**, 411, doi:[10.1029/TE044i004p00411](https://doi.org/10.1029/TE044i004p00411).
- 655 Blagau, A., I. Dandouras, A. Barthe, S. Brunato, G. Facskó, and V. Constanti-
 656 nescu (2013), In-flight calibration of Hot Ion Analyser onboard Cluster, *Geo-
 657 scientific Instrumentation, Methods and Data Systems Discussions*, **3**, 407–435,
 658 doi:[10.5194/gid-3-407-2013](https://doi.org/10.5194/gid-3-407-2013).
- 659 Blagau, A., I. Dandouras, A. Barthe, S. Brunato, G. Facskó, and V. Constantinescu

- 660 (2014), In-flight calibration of the Hot Ion Analyser on board Cluster, *Geoscientific Instrumentation, Methods and Data Systems*, *3*, 49–58, doi:10.5194/gi-3-49-
661 2014.
- 662 Chittenden, J. P., S. V. Lebedev, C. A. Jennings, S. N. Bland , and A. Ciardi
663 (2004), X-ray generation mechanisms in three-dimensional simulations of wire
664 array Z-pinches, *Plasma Physics and Controlled Fusion*, *46*(12B), B457–B476,
665 doi:10.1088/0741-3335/46/12B/039.
- 666 Ciardi, A., S. V. Lebedev, A. Frank, E. G. Blackman, J. P. Chittenden, C. J. Jen-
667 nings, D. J. Ampleford, S. N. Bland, S. C. Bott, J. Rapley, G. N. Hall, F. A.
668 Suzuki-Vidal, A. Marocchino, T. Lery, and C. Stehle (2007), The evolution of
669 magnetic tower jets in the laboratory, *Physics of Plasmas*, *14*(5), 056,501–056,501,
670 doi:10.1063/1.2436479.
- 671 Credland, J., G. Mecke, and J. Ellwood (1997), The Cluster Mission: ESA'S
672 Spacefleet to the Magnetosphere, *Space Science Reviews*, *79*, 33–64, doi:
673 10.1023/A:1004914822769.
- 674 Davis, T. N., and M. Sugiura (1966), Auroral electrojet activity index AE and its
675 universal time variations, *Journal of Geophysical Research*, *71*, 785–801, doi:
676 10.1029/JZ071i003p00785.
- 677 Décréau, P. M. E., P. Fergeau, V. Krasnoselskikh, E. Le Guiriec, M. Lévéque,
678 P. Martin, O. Randriamboarison, J. L. Rauch, F. X. Sené, H. C. Séran, J. G.
679 Trotignon, P. Canu, N. Cornilleau, H. de Féraudy, H. Alleyne, K. Yearby, P. B.
680 Mögensen, G. Gustafsson, M. André, D. C. Gurnett, F. Darrouzet, J. Lemaire,
681 C. C. Harvey, P. Travnicek, and Whisper Experimenters Group (2001), Early re-
682 sults from the Whisper instrument on Cluster: an overview, *Annales Geophysicae*,
683 *19*, 1241–1258, doi:10.5194/angeo-19-1241-2001.
- 684 Escoubet, C. P., M. Fehringer, and M. Goldstein (2001), Introduction The Cluster
685 mission, *Annales Geophysicae*, *19*, 1197–1200, doi:10.5194/angeo-19-1197-2001.
- 686 Facskó, G., I. Honkonen, T. Živković, L. Palin, E. Kallio, K. Ågren, H. Opgenoorth,
687 E. I. Tanskanen, and S. Milan (2016), One year in the Earth's magnetosphere: A
688 global MHD simulation and spacecraft measurements, *Space Weather*, *14*, 351–
689 367, doi:10.1002/2015SW001355.
- 690 Facskó, G., T. B. Balogh, E. I. Anekallu, C. R.and Tanskanen, P. Peitso, L. Degener,
691 M. Kangwa, T. Laitinen, and S. Laakso, H. Burley (in preparation), Bow shock

- identification in cluster measurements, *Space Weather*.
- Fazakerley, A. N., A. D. Lahiff, R. J. Wilson, I. Rozum, C. Anekallu, M. West, and H. Bacai (2010a), PEACE Data in the Cluster Active Archive, *Astrophysics and Space Science Proceedings*, 11, 129–144, doi:10.1007/978-90-481-3499-1_8.
- Fazakerley, A. N., A. D. Lahiff, I. Rozum, D. Kataria, H. Bacai, C. Anekallu, M. West, and A. Åsnes (2010b), Cluster-PEACE In-flight Calibration Status, *Astrophysics and Space Science Proceedings*, 11, 281–299, doi:10.1007/978-90-481-3499-1_19.
- García, K. S., and W. J. Hughes (2007), Finding the Lyon-Fedder-Mobarry magnetopause: A statistical perspective, *Journal of Geophysical Research (Space Physics)*, 112(A6), A06229, doi:10.1029/2006JA012039.
- Gordeev, E., G. Facskó, V. Sergeev, I. Honkonen, M. Palmroth, P. Janhunen, and S. Milan (2013), Verification of the GUMICS-4 global MHD code using empirical relationships, *Journal of Geophysical Research (Space Physics)*, 118, 3138–3146, doi:10.1002/jgra.50359.
- Greenwald, R. A., K. B. Baker, J. R. Dudeney, M. Pinnock, T. B. Jones, E. C. Thomas, J.-P. Villain, J.-C. Cerisier, C. Senior, C. Hanuise, R. D. Hunsucker, G. Sofko, J. Koehler, E. Nielsen, R. Pellinen, A. D. M. Walker, N. Sato, and H. Yamagishi (1995), Darn/Superdarn: A Global View of the Dynamics of High-Latitude Convection, *Space Science Reviews*, 71, 761–796, doi:10.1007/BF00751350.
- Guild, T. B., H. E. Spence, E. L. Kepko, V. Merkin, J. G. Lyon, M. Wiltberger, and C. C. Goodrich (2008a), Geotail and LFM comparisons of plasma sheet climatology: 1. Average values, *Journal of Geophysical Research (Space Physics)*, 113, A04216, doi:10.1029/2007JA012611.
- Guild, T. B., H. E. Spence, E. L. Kepko, V. Merkin, J. G. Lyon, M. Wiltberger, and C. C. Goodrich (2008b), Geotail and LFM comparisons of plasma sheet climatology: 2. Flow variability, *Journal of Geophysical Research (Space Physics)*, 113, A04217, doi:10.1029/2007JA012613.
- Gustafsson, G., R. Bostrom, B. Holback, G. Holmgren, A. Lundgren, K. Stasiewicz, L. Ahlen, F. S. Mozer, D. Pankow, P. Harvey, P. Berg, R. Ulrich, A. Pedersen, R. Schmidt, A. Butler, A. W. C. Fransen, D. Klinge, M. Thomsen, C.-G. Falthammar, P.-A. Lindqvist, S. Christenson, J. Holtet, B. Lybekk, T. A. Sten, P. Tan-

- 726 skanen, K. Lappalainen, and J. Wygant (1997), The Electric Field and Wave
727 Experiment for the Cluster Mission, *Space Science Reviews*, 79, 137–156, doi:
728 10.1023/A:1004975108657.
- 729 Gustafsson, G., M. André, T. Carozzi, A. I. Eriksson, C.-G. Fälthammar, R. Grard,
730 G. Holmgren, J. A. Holtet, N. Ivchenko, T. Karlsson, Y. Khotyaintsev, S. Klimov,
731 H. Laakso, P.-A. Lindqvist, B. Lybekk, G. Marklund, F. Mozer, K. Mursula,
732 A. Pedersen, B. Popielawska, S. Savin, K. Stasiewicz, P. Tanskanen, A. Vaivads,
733 and J.-E. Wahlund (2001), First results of electric field and density observations
734 by Cluster EFW based on initial months of operation, *Annales Geophysicae*, 19,
735 1219–1240, doi:10.5194/angeo-19-1219-2001.
- 736 Haiducek, J. D., D. T. Welling, N. Y. Ganushkina, S. K. Morley, and D. S. Oz-
737 turk (2017), SWMF Global Magnetosphere Simulations of January 2005: Geo-
738 magnetic Indices and Cross-Polar Cap Potential, *Space Weather*, 15, 1567–1587,
739 doi:10.1002/2017SW001695.
- 740 Iyemori, T. (1990), Storm-time magnetospheric currents inferred from mid-latitude
741 geomagnetic field variations, *Journal of Geomagnetism and Geoelectricity*, 42,
742 1249–1265, doi:10.5636/jgg.42.1249.
- 743 Janhunen, P., M. Palmroth, T. Laitinen, I. Honkonen, L. Juusola, G. Facskó, and
744 T. I. Pulkkinen (2012), The GUMICS-4 global MHD magnetosphere-ionosphere
745 coupling simulation, *Journal of Atmospheric and Solar-Terrestrial Physics*, 80,
746 48–59, doi:10.1016/j.jastp.2012.03.006.
- 747 Johnstone, A. D., C. Alsop, S. Burge, P. J. Carter, A. J. Coates, A. J. Coker, A. N.
748 Fazakerley, M. Grande, R. A. Gowen, C. Gurgiolo, B. K. Hancock, B. Narheim,
749 A. Preece, P. H. Sheather, J. D. Winningham, and R. D. Woodliffe (1997), Peace:
750 a Plasma Electron and Current Experiment, *Space Science Reviews*, 79, 351–398,
751 doi:10.1023/A:1004938001388.
- 752 Juusola, L., O. Amm, K. Kauristie, and A. Viljanen (2007), A model for estimating
753 the relation between the Hall to Pedersen conductance ratio and ground magnetic
754 data derived from CHAMP satellite statistics, *Annales Geophysicae*, 25, 721–736,
755 doi:10.5194/angeo-25-721-2007.
- 756 Juusola, L., G. Facskó, I. Honkonen, P. Janhunen, H. Vanhamäki, K. Kauristie,
757 T. V. Laitinen, S. E. Milan, M. Palmroth, E. I. Tanskanen, and A. Viljanen
758 (2014), Statistical comparison of seasonal variations in the GUMICS-4 global

- 759 MHD model ionosphere and measurements, *Space Weather*, 12, 582–600, doi:
760 10.1002/2014SW001082.
- 761 Kallio, E., and G. Facskó (2015), Properties of plasma near the moon in the magne-
762 total, *Planetary and Space Science*, 115, 69–76, doi:10.1016/j.pss.2014.11.007.
- 763 Kokubun, S., T. Yamamoto, M. H. Acuña, K. Hayashi, K. Shiokawa, and H. Kawano
764 (1994), The GEOTAIL Magnetic Field Experiment., *Journal of Geomagnetism*
765 and *Geoelectricity*, 46, 7–21, doi:10.5636/jgg.46.7.
- 766 Lakka, A., T. I. Pulkkinen, A. P. Dimmock, M. Myllys, I. Honkonen, and M. Palm-
767 roth (2018a), The Cross-Polar Cap Saturation in GUMICS-4 During High Solar
768 Wind Driving, *Journal of Geophysical Research (Space Physics)*, 123, 3320–3332,
769 doi:10.1002/2017JA025054.
- 770 Lakka, A., T. I. Pulkkinen, A. P. Dimmock, E. Kilpuu, M. Ala-Lahti, I. Honko-
771 nen, M. Palmroth, and Raukunen (2018b), Icme impact at earth with low and
772 typical mach number plasma characteristics, *Annales Geophysicae Discussions*,
773 <https://doi.org/10.5194/angeo-2018-81>.
- 774 Lani, A., A. Sanna, N. Villedieu, and M. Panesi (2012), COOLFluiD an Open Com-
775 putational Platform for Aerothermodynamics and Flow-Radiation Coupling, in
776 *ESA Special Publication, ESA Special Publication*, vol. 714, p. 45.
- 777 Liemohn, M., N. Y. Ganushkina, D. L. De Zeeuw, L. Rastaetter, M. Kuznetsova,
778 D. T. Welling, G. Toth, R. Ilie, T. I. Gombosi, and B. van der Holst (2018), Real-
779 Time SWMF at CCMC: Assessing the Dst Output From Continuous Operational
780 Simulations, *Space Weather*, 16(10), 1583–1603, doi:10.1029/2018SW001953.
- 781 Lyon, J. G., J. A. Fedder, and C. M. Mobarry (2004), The Lyon-Fedder-Mobarry
782 (LFM) global MHD magnetospheric simulation code, *Journal of Atmospheric and*
783 *Solar-Terrestrial Physics*, 66, 1333–1350, doi:10.1016/j.jastp.2004.03.020.
- 784 Mejnertsen, L., J. P. Eastwood, J. P. Chittenden, and A. Masters (2016), Global
785 MHD simulations of Neptune’s magnetosphere, *Journal of Geophysical Research*
786 (*Space Physics*), 121(8), 7497–7513, doi:10.1002/2015JA022272.
- 787 Mejnertsen, L., J. P. Eastwood, H. Hietala, S. J. Schwartz, and J. P. Chittenden
788 (2018), Global MHD Simulations of the Earth’s Bow Shock Shape and Motion
789 Under Variable Solar Wind Conditions, *Journal of Geophysical Research (Space*
790 *Physics*), 123(1), 259–271, doi:10.1002/2017JA024690.
- 791 Mukai, T., S. Machida, Y. Saito, M. Hirahara, T. Terasawa, N. Kaya, T. Obara,

- 792 M. Ejiri, and A. Nishida (1994), The Low Energy Particle (LEP) Experiment on-
793 board the GEOTAIL Satellite., *Journal of Geomagnetism and Geoelectricity*, *46*,
794 669–692, doi:10.5636/jgg.46.669.
- 795 Peredo, M., J. A. Slavin, E. Mazur, and S. A. Curtis (1995), Three-dimensional po-
796 sition and shape of the bow shock and their variation with Alfvénic, sonic and
797 magnetosonic Mach numbers and interplanetary magnetic field orientation, *Jour-*
798 *nal of Geophysical Research*, *100*, 7907–7916, doi:10.1029/94JA02545.
- 799 Poedts, S., A. Kochanov, A. Lani, C. Scolini, C. Verbeke, S. Hosteaux, E. Chané,
800 H. Deconinck, N. Mihalache, F. Diet, D. Heynderickx, J. De Keyser, E. De
801 Donder, N. B. Crosby, M. Echim, L. Rodriguez, R. Vansintjan, F. Verstringe,
802 B. Mampaey, R. Horne, S. Glauert, P. Jiggens, R. Keil, A. Glover, G. Deprez, and
803 J.-P. Luntama (2020), The Virtual Space Weather Modelling Centre, *Journal of*
804 *Space Weather and Space Climate*, *10*, 14, doi:10.1051/swsc/2020012.
- 805 Powell, K. G., P. L. Roe, T. J. Linde, T. I. Gombosi, and D. L. De Zeeuw (1999), A
806 Solution-Adaptive Upwind Scheme for Ideal Magnetohydrodynamics, *Journal of*
807 *Computational Physics*, *154*, 284–309, doi:10.1006/jcph.1999.6299.
- 808 Raeder, J., D. Larson, W. Li, E. L. Kepko, and T. Fuller-Rowell (2008), OpenG-
809 GCM Simulations for the THEMIS Mission, *Space Science Reviews*, *141*, 535–555,
810 doi:10.1007/s11214-008-9421-5.
- 811 Reigber, C., H. Lühr, and P. Schwintzer (2002), CHAMP mission status, *Advances*
812 *in Space Research*, *30*, 129–134, doi:10.1016/S0273-1177(02)00276-4.
- 813 Reme, H., J. M. Bosqued, J. A. Sauvaud, A. Cros, J. Dandouras, C. Aoustin,
814 J. Bouyssou, T. Camus, J. Cuvilo, C. Martz, J. L. Medale, H. Perrier, D. Rome-
815 fort, J. Rouzaud, C. D'Uston, E. Mobius, K. Crocker, M. Granoff, L. M. Kistler,
816 M. Popecki, D. Hovestadt, B. Klecker, G. Paschmann, M. Scholer, C. W. Carl-
817 son, D. W. Curtis, R. P. Lin, J. P. McFadden, V. Formisano, E. Amata, M. B.
818 Bavassano-Cattaneo, P. Baldetti, G. Belluci, R. Bruno, G. Chionchio, A. di Lel-
819 lis, E. G. Shelley, A. G. Ghielmetti, W. Lennartsson, A. Korth, H. Rosenbauer,
820 R. Lundin, S. Olsen, G. K. Parks, M. McCarthy, and H. Balsiger (1997), The
821 Cluster Ion Spectrometry (CIS) Experiment, *Space Science Reviews*, *79*, 303–350,
822 doi:10.1023/A:1004929816409.
- 823 Rème, H., C. Aoustin, J. M. Bosqued, I. Dandouras, B. Lavraud, J. A. Sauvaud,
824 A. Barthe, J. Bouyssou, T. Camus, O. Coeur-Joly, A. Cros, J. Cuvilo, F. Ducay,

- 825 Y. Garbarowitz, J. L. Medale, E. Penou, H. Perrier, D. Romefort, J. Rouzaud,
 826 C. Vallat, D. Alcayde, C. Jacquay, C. Mazelle, C. D'Uston, E. Mobius, L. M.
 827 Kistler, K. Crocker, M. Granoff, C. Mouikis, M. Popecki, M. Vosbury, B. Klecker,
 828 D. Hovestadt, H. Kucharek, E. Kuenneth, G. Paschmann, M. Scholer, N. Sckopke,
 829 E. Seidenschwang, C. W. Carlson, D. W. Curtis, C. Ingraham, R. P. Lin, J. P.
 830 McFadden, G. K. Parks, T. Phan, V. Formisano, E. Amata, M. B. Bavassano-
 831 Cattaneo, P. Baldetti, R. Bruno, G. Chionchio, A. di Lellis, M. F. Marcucci,
 832 G. Pallocchia, A. Korth, P. W. Daly, B. Graeve, H. Rosenbauer, V. Vasylunas,
 833 M. McCarthy, M. Wilber, L. Eliasson, R. Lundin, S. Olsen, E. G. Shelley, S. Fuseli-
 834 er, A. G. Ghielmetti, W. Lennartsson, C. P. Escoubet, H. Balsiger, R. Friedel, J.-
 835 B. Cao, R. A. Kovrashkin, I. Papamastorakis, R. Pellat, J. Scudder, and B. Son-
 836 nerup (2001), First multispacecraft ion measurements in and near the Earth's
 837 magnetosphere with the identical Cluster ion spectrometry (CIS) experiment,
 838 *Annales Geophysicae*, 19, 1303–1354, doi:10.5194/angeo-19-1303-2001.
- 839 Ritter, P., H. Luhrl, A. Viljanen, O. Amm, A. Pulkkinen, and I. Sillanpaa (2004),
 840 Ionospheric currents estimated simultaneously from CHAMP satelliteand IMAGE
 841 ground-based magnetic field measurements: a statisticalstudy at auroral latitudes,
 842 *Annales Geophysicae*, 22, 417–430, doi:10.5194/angeo-22-417-2004.
- 843 Rostoker, G. (1972), Geomagnetic indices., *Reviews of Geophysics and Space
 844 Physics*, 10, 935–950, doi:10.1029/RG010i004p00935.
- 845 Siscoe, G. L., G. M. Erickson, B. U. Sonnerup, N. C. Maynard, J. A. Schoendorf,
 846 K. D. Siebert, D. R. Weimer, W. W. White, and G. R. Wilson (2001), The Mag-
 847 netospheric Fluopause, in *AGU Spring Meeting Abstracts*, vol. 2001, pp. SM52D–
 848 02.
- 849 Sofko, G. J., R. Greenwald, and W. Bristow (1995), Direct determination of large-
 850 scale magnetospheric field-aligned currents with SuperDARN, *Geophysical Re-
 851 search Letters*, 22, 2041–2044, doi:10.1029/95GL01317.
- 852 Thomsen, M. F. (2004), Why Kp is such a good measure of magnetospheric convec-
 853 tion, *Space Weather*, 2, S11004, doi:10.1029/2004SW000089.
- 854 Toth, G., I. V. Sokolov, T. I. Gombosi, D. R. Chesney, C. R. Clauer, D. L. de
 855 Zeeuw, K. C. Hansen, K. J. Kane, W. B. Manchester, R. C. Oehmke, K. G. Pow-
 856 ell, A. J. Ridley, I. I. Roussev, Q. F. Stout, O. Volberg, R. A. Wolf, S. Sazykin,
 857 A. Chan, B. Yu, and J. Kota (2005), Space Weather Modeling Framework: A

- 858 new tool for the space science community, *Journal of Geophysical Research (Space*
859 *Physics)*, 110, A12226, doi:10.1029/2005JA011126.
- 860 Tóth, G., B. van der Holst, I. V. Sokolov, D. L. De Zeeuw, T. I. Gombosi, F. Fang,
861 W. B. Manchester, X. Meng, D. Najib, K. G. Powell, Q. F. Stout, A. Glo-
862 cer, Y.-J. Ma, and M. Opher (2012), Adaptive numerical algorithms in space
863 weather modeling, *Journal of Computational Physics*, 231, 870–903, doi:
864 10.1016/j.jcp.2011.02.006.
- 865 Trotignon, J. G., P. M. E. Décréau, J. L. Rauch, X. Vallières, A. Rochel,
866 S. Kougblénou, G. Lointier, G. Facskó, P. Canu, F. Darrouzet, and A. Masson
867 (2010), The WHISPER Relaxation Sounder and the CLUSTER Active Archive,
868 *Astrophysics and Space Science Proceedings*, 11, 185–208, doi:10.1007/978-90-481-
869 3499-1_12.
- 870 Trotignon, J.-G., Vallières, and the WHISPER team (2011), Calibration report of
871 the whisper measurements in the cluster active archive (caa), *Tech. rep.*, LPC2E
872 CNRS, caa-est-cr-whi.
- 873 Tsyganenko, N. A. (1995), Modeling the Earth's magnetospheric magnetic field
874 confined within a realistic magnetopause, *Journal of Geophysical Research*, 100,
875 5599–5612, doi:10.1029/94JA03193.
- 876 Vörös, Z., G. Facskó, M. Khodachenko, I. Honkonen, P. Janhunen, and M. Palmroth
877 (2014), Windsock memory COnditioned RAM (CO-RAM) pressure effect: Forced
878 reconnection in the Earth's magnetotail, *Journal of Geophysical Research (Space*
879 *Physics)*, 119, 6273–6293, doi:10.1002/2014JA019857.
- 880 Wang, Z.-D., and R. L. Xu (1994), Signatures of the magnetotail neutral sheet,
881 *Geophysical Research Letters*, 21(19), 2087–2090, doi:10.1029/94GL01960.
- 882 Weimer, D. R. (2005), Improved ionospheric electrodynamic models and applica-
883 tion to calculating Joule heating rates, *Journal of Geophysical Research (Space*
884 *Physics)*, 110, A05306, doi:10.1029/2004JA010884.
- 885 Wiltberger, M., E. J. Rigler, V. Merkin, and J. G. Lyon (2017), Structure of High
886 Latitude Currents in Magnetosphere-Ionosphere Models, *Space Science Reviews*,
887 206, 575–598, doi:10.1007/s11214-016-0271-2.
- 888 Zhang, B., W. Lotko, M. J. Wiltberger, O. J. Brambles, and P. A. Damiano (2011),
889 A statistical study of magnetosphere-ionosphere coupling in the Lyon-Fedder-
890 Mobarry global MHD model, *Journal of Atmospheric and Solar-Terrestrial*

- 891 *Physics*, 73, 686–702, doi:10.1016/j.jastp.2010.09.027.
- 892 Zhang, B., K. A. Sorathia, J. G. Lyon, V. G. Merkin, J. S. Garretson, and M. Wilt-
- 893 berger (2019), GAMERA: A Three-dimensional Finite-volume MHD Solver for
- 894 Non-orthogonal Curvilinear Geometries, *The Astrophysical Journal Supplement*
- 895 *Series*, 244(1), 20, doi:10.3847/1538-4365/ab3a4c.

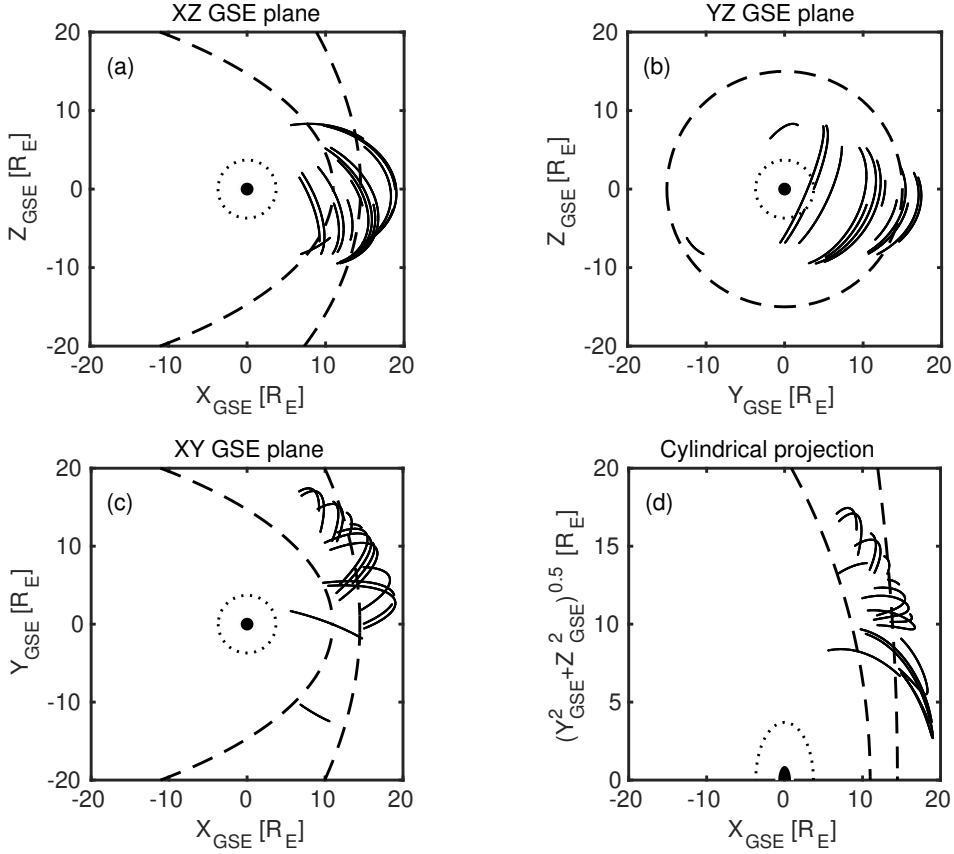


Figure 1. Cluster SC3 orbit in the solar wind in GSE system for all intervals (see Table 1).
 (a) XZ (b) YZ (c) XY (d) Cylindrical projection. Average bow-shock and magnetopause positions are drawn on all plots using dashed lines [Perego *et al.*, 1995; Tsyganenko, 1995, respectively]. The black dots at $3.7 R_E$ show the boundary of the GUMICS-4 inner magnetospheric domain. The black circle in the origo of all plots shows the size of the Earth.

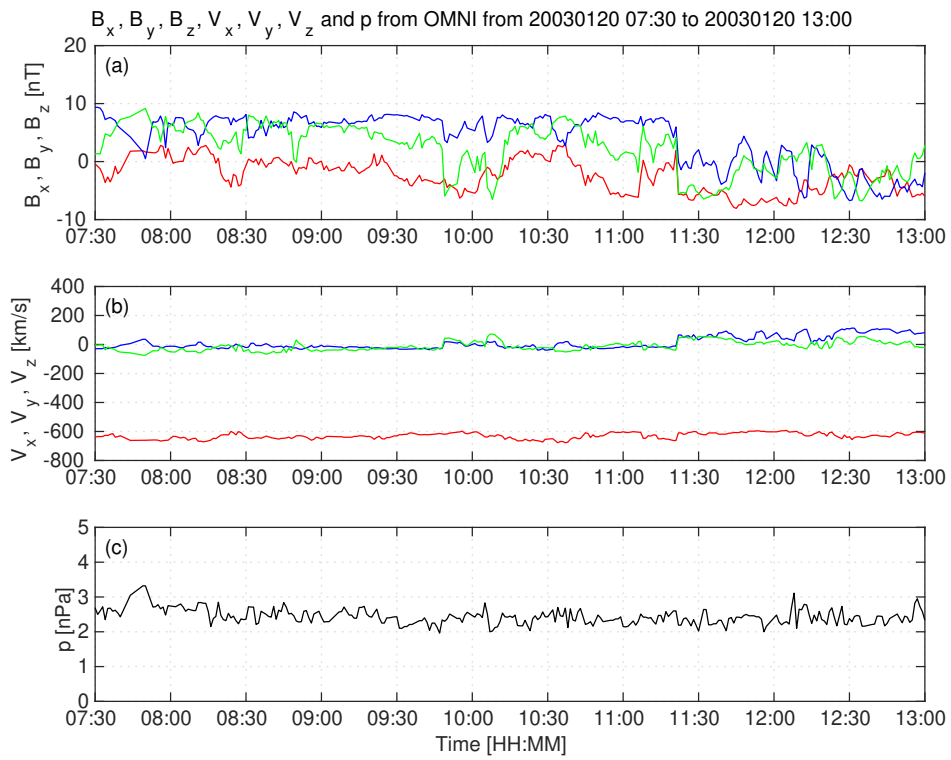
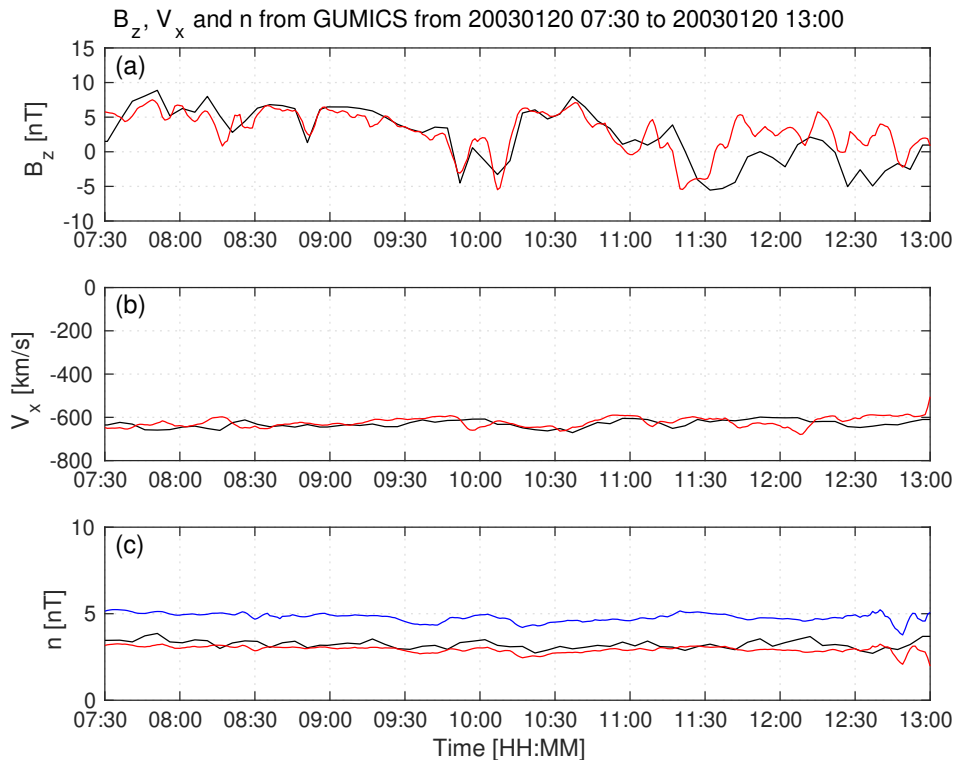
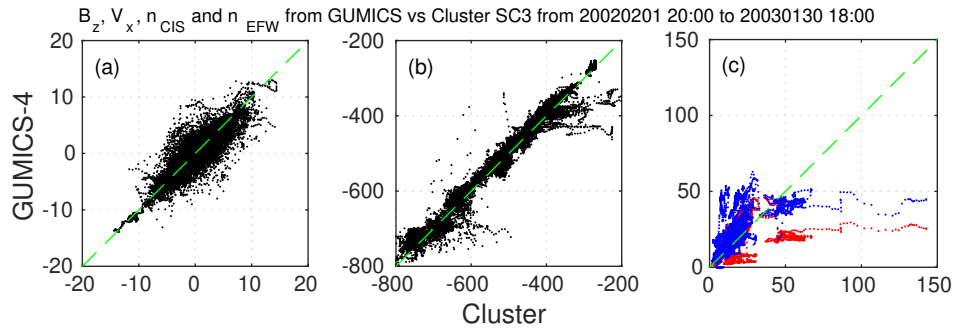


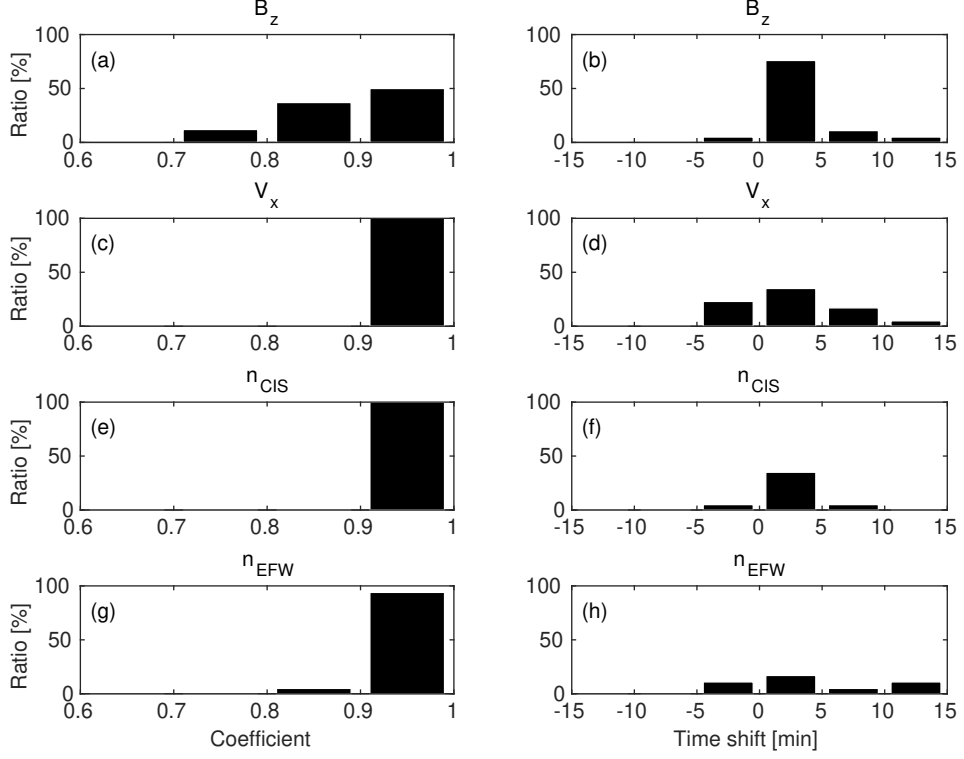
Figure 2. OMNI solar wind data in GSE system from 7:30 to 13:00 (UT) on January 20, 2003. (a) Magnetic field B_x (red), B_y (green) and B_z (blue) components. (b) Solar wind velocity V_x (red), V_y (green) and V_z (blue) components. (c) The P pressure of the solar wind (black).



904 **Figure 3.** GUMICS-4 simulation results (black) and Cluster SC3 magnetic field Z component,
905 ion plasma moments (red) and electron density calculated from spacecraft potential (blue) from
906 January 20, 2003 from 7:30 to 13:00 (UT) in the solar wind in GSE system. (a) Magnetic field Z
907 component. (b) Solar wind velocity X component (c) Solar wind density.



908 **Figure 4.** Scattered plots of the Cluster SC3 and GUMICS-4 simulations for all intervals in
 909 the solar wind. The dashed line is the $y=x$ line. (a) Magnetic field Z component in GSE system.
 910 (b) Solar wind velocity X component in GSE system. (c) Solar wind density measured by the
 911 CIS HIA instrument (red) and calculated from the spacecraft potential (blue).



912 **Figure 5.** The distributions of the highest correlation coefficients (a, c, e, g) of the magnetic
 913 field Z component (B_z) in GSE system, solar wind velocity X component (V_x) in GSE system,
 914 the solar wind density measured by the CIS HIA (n_{CIS}) instrument and calculated from the
 915 spacecraft potential (n_{EFW}), respectively, for all intervals in the solar wind. The distributions
 916 of the corresponding time shifts (b, d, f, h) of the B_z , the V_x , the n_{CIS} and the n_{EFW}), respec-
 917 tively, for all intervals in the solar wind.

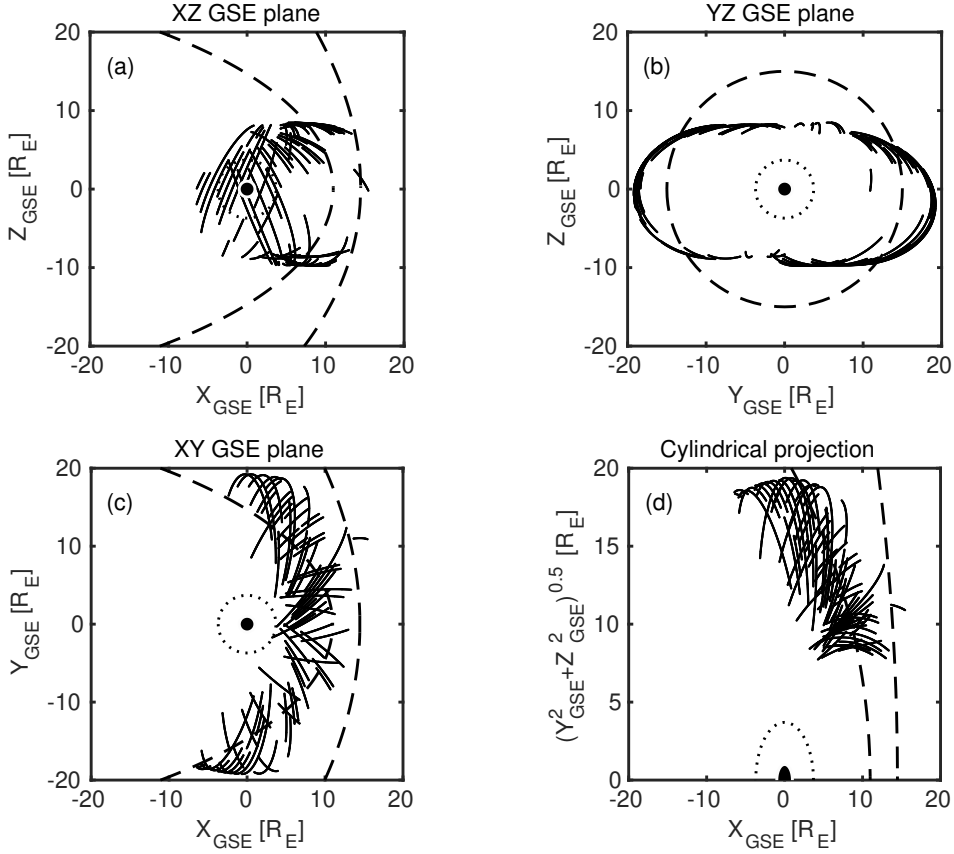
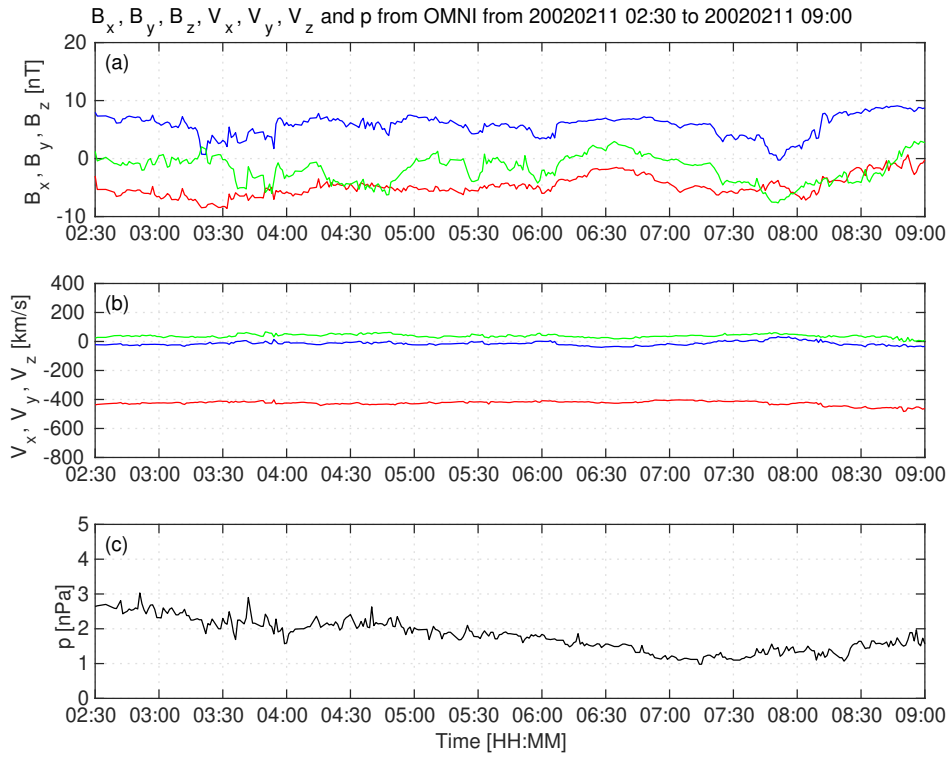
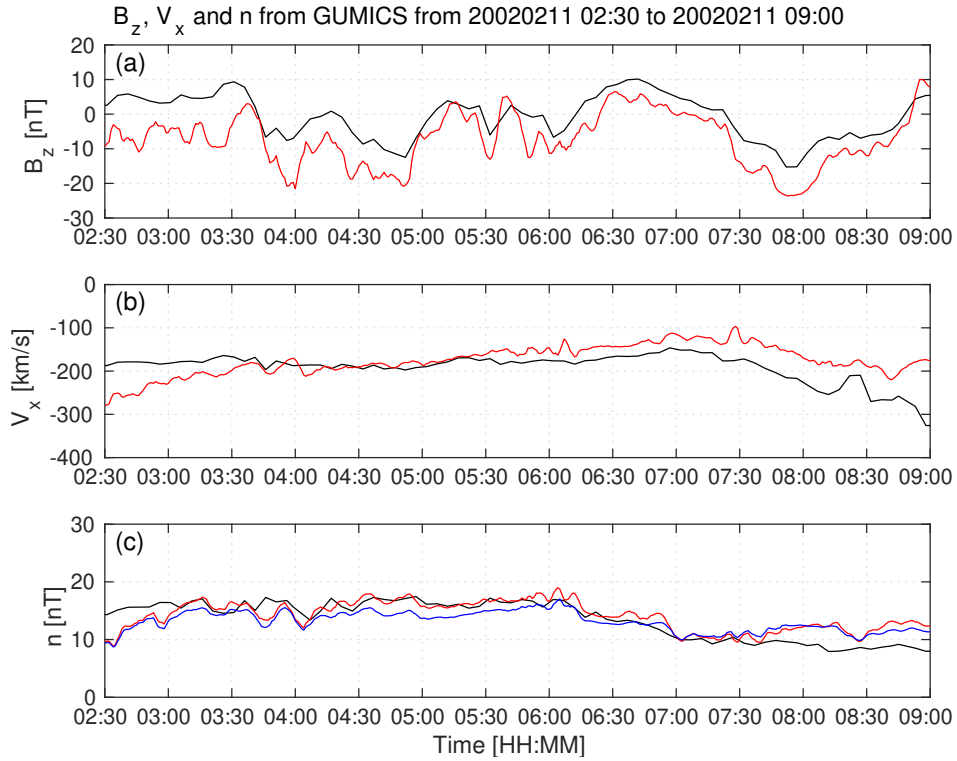


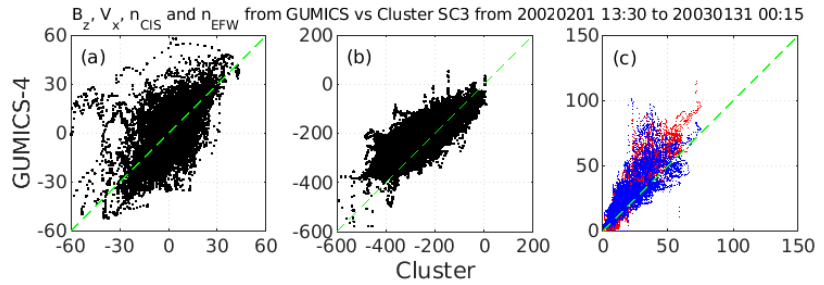
Figure 6. Cluster SC3 orbit in the magnetosheath in GSE system for all intervals (see Table 2). (a) XZ (b) YZ (c) XY (d) Cylindrical projection. Average bow-shock and magnetopause positions are drawn on all plots using dashed lines [Perez et al., 1995; Tsyganenko, 1995, respectively]. The black dots at $3.7 R_E$ show the boundary of the GUMICS-4 inner magnetospheric domain. The black circle in the origo of all plots shows the size of the Earth.



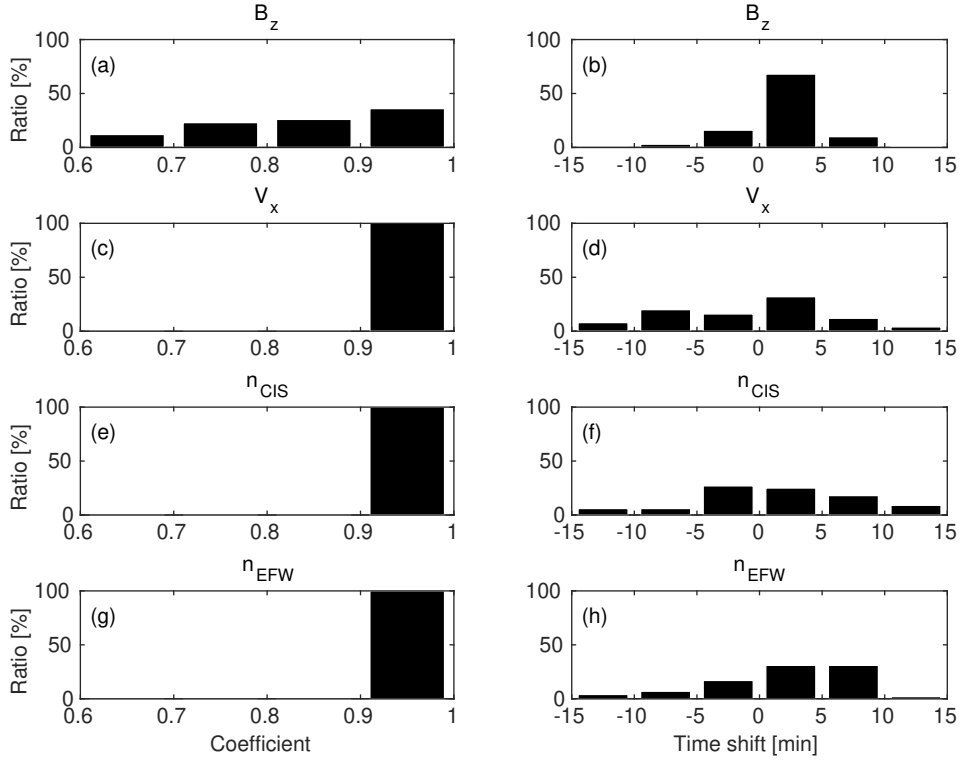
923 **Figure 7.** OMNI solar wind data in GSE system from 2:30 to 09:00 (UT) on February 11,
924 2002. (a) Magnetic field B_x (red), B_y (green) and B_z (blue) components. (b) Solar wind velocity
925 V_x (red), V_y (green) and V_z (blue) components. (c) The P pressure of the solar wind (black).



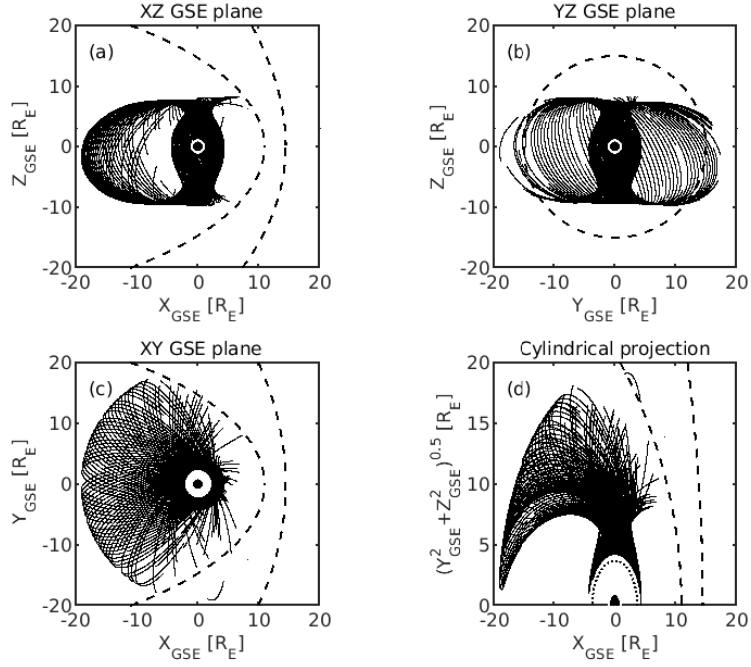
926 **Figure 8.** GUMICS-4 simulation results (black) and Cluster SC3 magnetic field Z component,
927 ion plasma moments (red) and electron density calculated from spacecraft potential (blue) from
928 February 11, 2002 from 2:30 to 9:00 (UT) in the magnetosheath in GSE system (a) Magnetic
929 field Z component. (b) Solar wind velocity X component (c) Solar wind density.



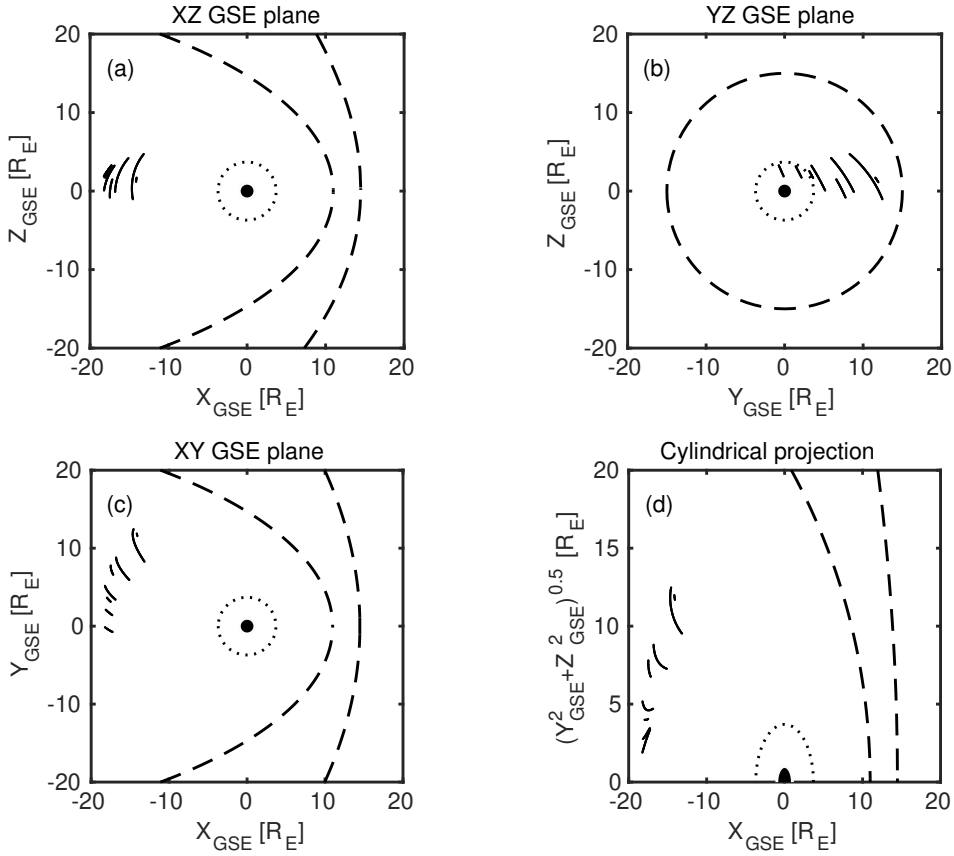
930 **Figure 9.** Scattered plots of the Cluster SC3 and GUMICS–4 simulations for all intervals in
 931 the magnetosheath in GSE system. The dashed line is the $y=x$ line. (a) Magnetic field Z com-
 932 ponent. (b) Solar wind velocity X component. (c) Solar wind density measured by the CIS HIA
 933 instrument (red) and calculated from the spacecraft potential (blue).



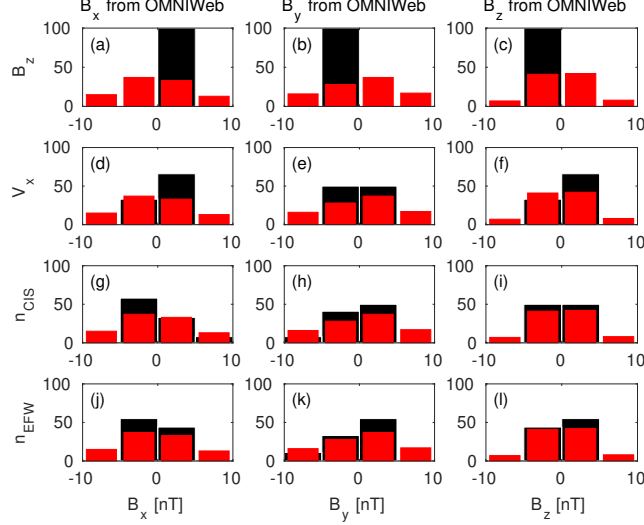
934 **Figure 10.** The distributions of the correlation coefficients (a, c, e, g) of the magnetic field Z
 935 component (B_z) in GSE system, solar wind velocity X component (V_x) in GSE system, the solar
 936 wind density measured by the CIS HIA (n_{CIS}) instrument and calculated from the spacecraft
 937 potential (n_{EFW}), respectively, for all intervals in the magnetosheath. The distributions of the
 938 time shifts (b, d, f, h) of the B_z , the V_x , the n_{CIS} and the n_{EFW}), respectively, for all intervals
 939 in the magnetosheath.



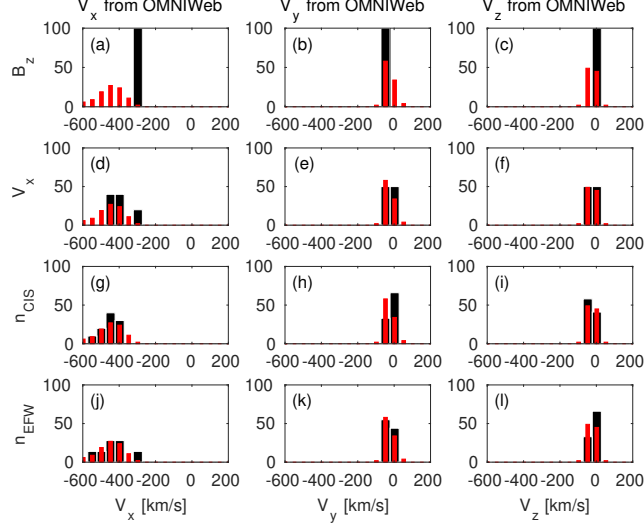
940 **Figure 11.** Cluster SC3 orbit in the magnetosphere in GSE system for all intervals (see Ta-
 941 ble 3). (a) XZ (b) YZ (c) XY (d) Cylindrical projection. Average bow-shock and magnetopause
 942 positions are drawn on all plots using dashed lines [Perego *et al.*, 1995; Tsyganenko, 1995, respec-
 943 tively]. The black dots at $3.7 R_E$ show the boundary of the GUMICS-4 inner magnetospheric
 944 domain. The black circle in the origo of all plots shows the size of the Earth.



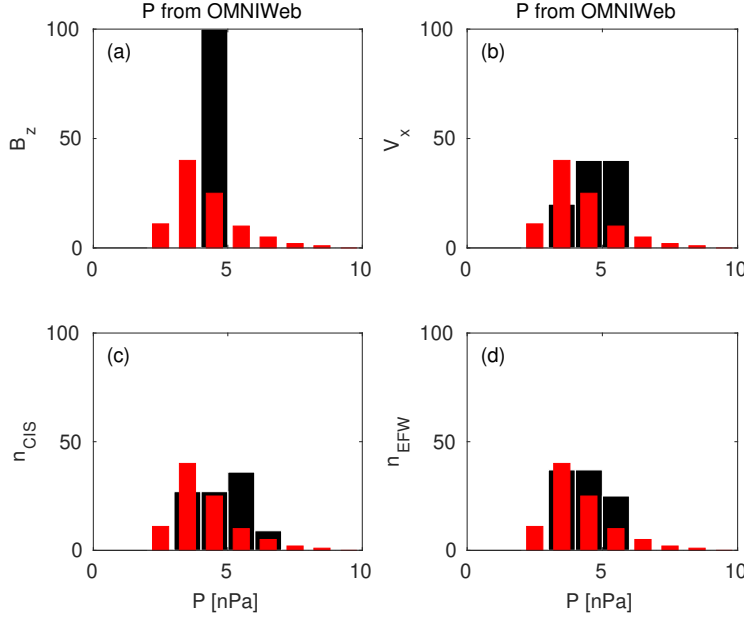
945 **Figure 12.** Cluster SC3 orbit in the tail in GSE system for all intervals (see Table 8). (a) XZ
 946 (b) YZ (c) XY (d) Cylindrical projection. Average bow-shock and magnetopause positions are
 947 drawn on all plots using dashed lines [Peredo *et al.*, 1995; Tsyganenko, 1995, respectively]. The
 948 black dots at $3.7 R_E$ show the boundary of the GUMICS-4 inner magnetospheric domain. The
 949 black circle in the origo of all plots shows the size of the Earth.



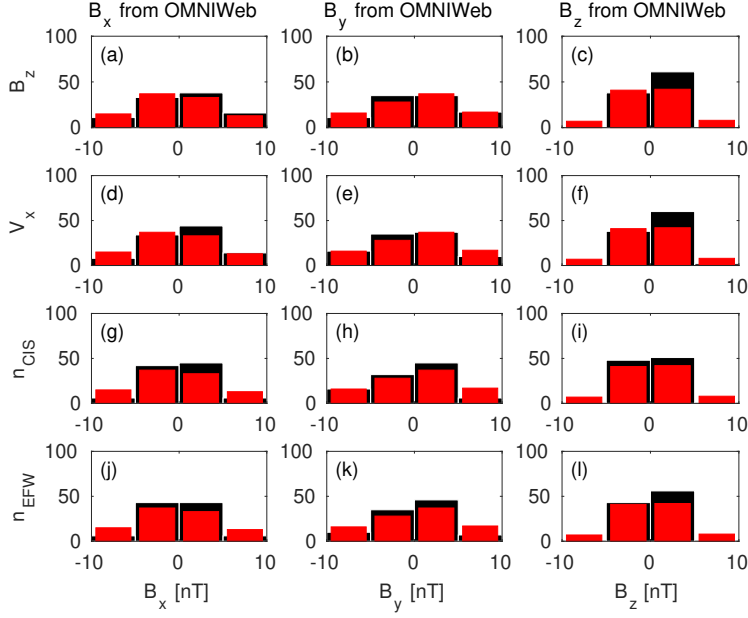
950 **Figure 13.** The black distributions of the B_x , the B_y and the B_z OMNI solar wind magnetic
 951 field components when the agreement of the Cluster SC3 measurements and the GUMICS-4
 952 simulations are poor in the solar wind (see Table 4). The B_z , the V_x , the n_{CIS} and the n_{EFW}
 953 are the magnetic field GSE Z component, the plasma ion velocity X GSE component, the solar
 954 wind density measured by the CIS HIA instrument and the calculated from the EFW spacecraft
 955 potential, respectively. (a, b, c) Distribution of OMNI B_x , B_y , B_z when the agreement of B_z
 956 is poor. (d, e, f) Distribution of OMNI B_x , B_y , B_z when the agreement of V_x is poor. (g, h, i)
 957 Distribution of OMNI B_x , B_y , B_z when the agreement of n_{CIS} is poor. (j, k, l) Distribution of
 958 OMNI B_x , B_y , B_z when the agreement of n_{EFW} is poor. The values are in percentage units in
 959 the distributions. The red distributions of (a, d, g, j), (b, e, h, k) and (c, f, i, l) are the distribu-
 960 tion of the B_x , the B_y , and the B_z components of the OMNI solar wind magnetic field during the
 961 1-year run from January 29, 2002, to February 2, 2003, in GSE reference frame, respectively.



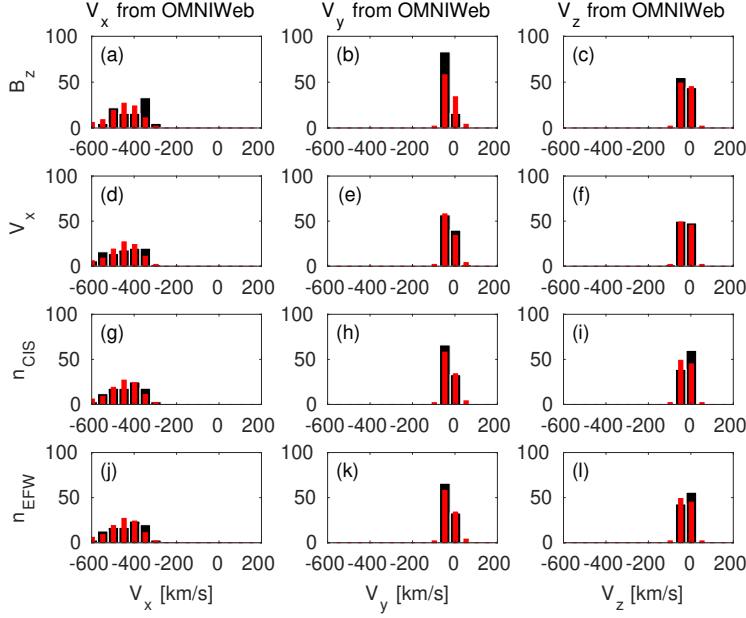
962 **Figure 14.** The black distributions of the V_x , the V_y and the V_z OMNI solar wind magnetic
 963 field components when the agreement of the Cluster SC3 measurements and the GUMICS–4
 964 simulations are poor in the solar wind (see Table 4). The B_z , the V_x , the n_{CIS} and the n_{EFW}
 965 are the magnetic field GSE Z component, the plasma ion velocity X GSE component, the solar
 966 wind density measured by the CIS HIA instrument and the calculated from the EFW spacecraft
 967 potential, respectively. (a, b, c) Distribution of OMNI V_x , V_y , V_z when the agreement of B_z is
 968 poor. (d, e, f) Distribution of OMNI V_x , V_y , V_z when the agreement of V_x is poor. (g, h, i) Dis-
 969 tribution of OMNI V_x , V_y , V_z when the agreement of n_{CIS} is poor. (j, k, l) Distribution of OMNI
 970 V_x , V_y , V_z when the agreement of n_{EFW} is poor. The values are in percentage unit in the distri-
 971 butions. The red distributions of (a, d, g, j), (b, e, h, k) and (c, f, i, l) are the distributions of the
 972 V_x , the V_y and the V_z components of the OMNI solar wind velocity during the 1-year run from
 973 January 29, 2002 to February 2, 2003 in GSE reference frame, respectively.



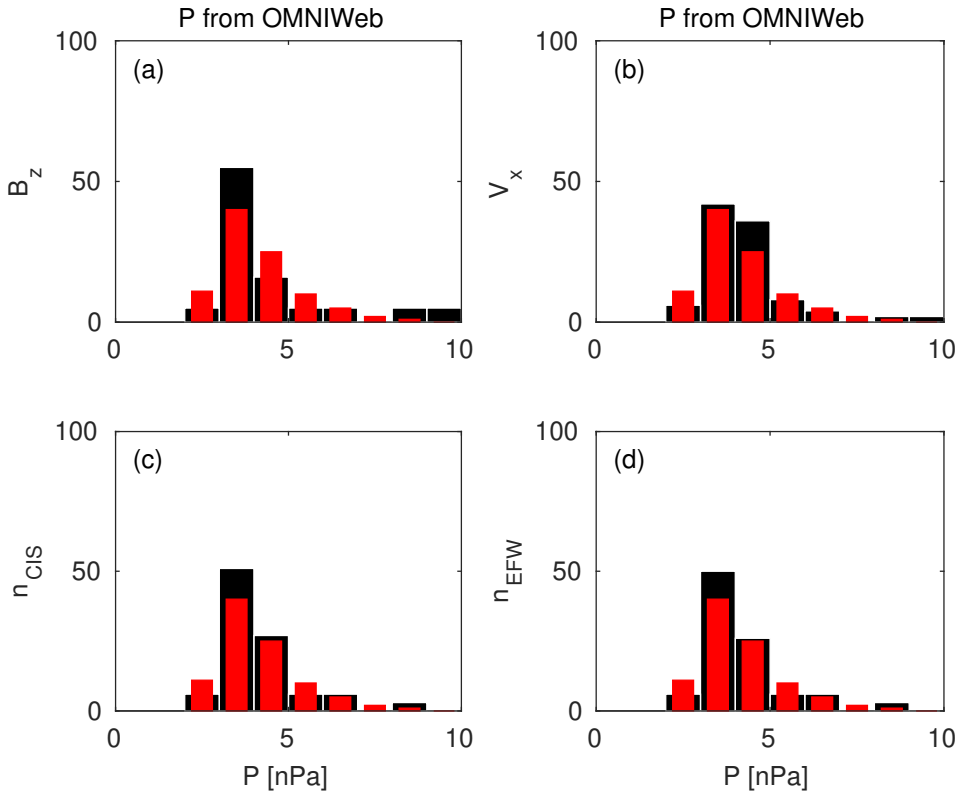
974 **Figure 15.** The black distributions of the P solar wind dynamic pressure calculated from
 975 OMNI parameters when the agreement of the Cluster SC3 measurements and the GUMICS-4
 976 simulations are poor in the solar wind (see Table 4). The B_z , V_x , n_{CIS} and n_{EFW} are the mag-
 977 netic field GSE Z component, the velocity X GSE component, the solar wind density measured
 978 by the CIS HIA instrument and calculated from the EFW spacecraft potential, respectively.
 979 (a, b, c, d) The distribution of the P calculated from OMNI data when the agreement of the B_z ,
 980 the V_x , the n_{CIS} or the n_{EFW} are poor. The values are in percentage unit in the distributions.
 981 The red distributions of (a, b, c, d) are the distributions of the P solar wind dynamic pressure
 982 calculated from the OMNI solar wind parameters during the 1-year run from January 29, 2002 to
 983 February 2, 2003 in GSE reference frame.



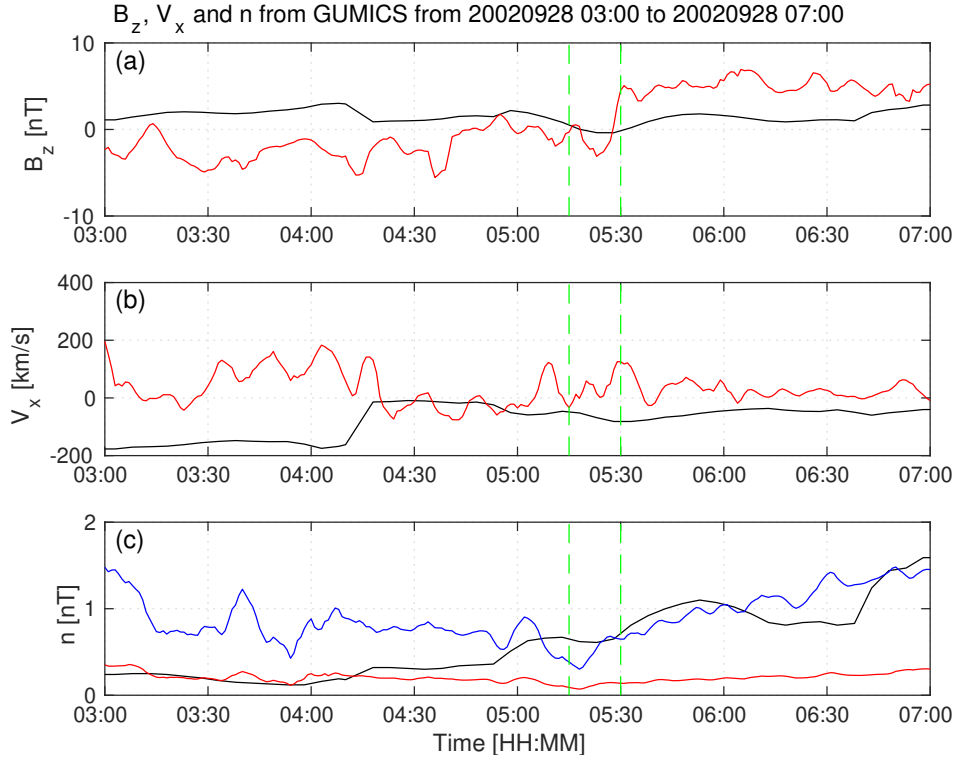
984 **Figure 16.** The black distributions of the B_x , the B_y and the B_z OMNI solar wind magnetic
985 field components when the agreement of the Cluster SC3 measurements and the GUMICS–4
986 simulations are poor in the magnetosheath (see Table 5). The B_z , the V_x , the n_{CIS} and the
987 n_{EFW} are the magnetic field GSE Z component, the plasma ion velocity X GSE component,
988 the solar wind density measured by the CIS HIA instrument and the calculated from the EFW
989 spacecraft potential, respectively. (a, b, c) Distribution of OMNI B_x , B_y , B_z when the agree-
990 ment of B_z is poor. (d, e, f) Distribution of OMNI B_x , B_y , B_z when the agreement of V_x is
991 poor. (g, h, i) Distribution of OMNI B_x , B_y , B_z when the agreement of n_{CIS} is poor. (j, k, l)
992 Distribution of OMNI B_x , B_y , B_z when the agreement of n_{EFW} is poor. The values are in per-
993 centage unit in the distributions. The red distributions of (a, d, g, j), (b, e, h, k) and (c, f, i, l)
994 are the distribution of the B_x , the B_y , and the B_z components of the OMNI solar wind magnetic
995 field during the 1-year run from January 29, 2002 to February 2, 2003 in GSE reference frame,
996 respectively.



997 **Figure 17.** The black distributions of the V_x , the V_y and the V_z OMNI solar wind magnetic
 998 field components when the agreement of the Cluster SC3 measurements and the GUMICS-4
 999 simulations are poor in the magnetosheath (see Table 5). The B_z , the V_x , the n_{CIS} and the
 1000 n_{EFW} are the magnetic field GSE Z component, the plasma ion velocity X GSE component, the
 1001 solar wind density measured by the CIS HIA instrument and the calculated from the EFW space-
 1002 craft potential, respectively. (a, b, c) Distribution of OMNI V_x , V_y , V_z when the agreement of
 1003 B_z is poor. (d, e, f) Distribution of OMNI V_x , V_y , V_z when the agreement of V_x is poor. (g, h, i)
 1004 Distribution of OMNI V_x , V_y , V_z when the agreement of n_{CIS} is poor. (j, k, l) Distribution of
 1005 OMNI V_x , V_y , V_z when the agreement of n_{EFW} is poor. The values are in percentage unit in the
 1006 distributions. The red distributions of (a, d, g, j), (b, e, h, k) and (c, f, i, l) are the distributions
 1007 of the V_x , the V_y and the V_z components of the OMNI solar wind velocity during the 1-year run
 1008 from January 29, 2002 to February 2, 2003 in GSE reference frame, respectively.



1009 **Figure 18.** The black distributions of the P solar wind dynamic pressure calculated from
 1010 OMNI parameters when the agreement of the Cluster SC3 measurements and the GUMICS–4
 1011 simulations are poor in the magnetosheath (see Table 5). The B_z , V_x , n_{CIS} and n_{EFW} are
 1012 the magnetic field GSE Z component, the velocity X GSE component, the solar wind density
 1013 measured by the CIS HIA instrument and calculated from the EFW spacecraft potential, respec-
 1014 tively. (a, b, c, d) The distribution of the P calculated from OMNI data when the agreement of
 1015 the B_z , the V_x , the n_{CIS} or the n_{EFW} are poor. The values are in percentage unit in the distri-
 1016 butions. The red distributions of (a, b, c, d) are the distributions of the P solar wind dynamic
 1017 pressure calculated from the OMNI solar wind parameters during the 1-year run from January
 1018 29, 2002 to February 2, 2003 in GSE reference frame.



1019 **Figure 19.** GUMICS-4 simulation results (black) and Cluster SC3 magnetic field Z compo-
 1020 nent, ion plasma moments (red) and electron density calculated from spacecraft potential (blue)
 1021 from September 28, 2002 from 3:00 to 7:00 (UT) in the tail in GSE system. (a) Magnetic field
 1022 Z component. (b) Solar wind velocity X component (c) Solar wind density. From 05:15 to 05:30
 1023 between the green dashed vertical lines both the Cluster SC3 and the virtual spaceprobe of the
 1024 GUMICS-4 simulation cross the neutral sheet multiple times.

Start/End	C_{B_z}	δt_{B_z}	C_{V_x}	δt_{V_x}	$C_{n_{CIS}}$	$\delta t_{n_{CIS}}$	$C_{n_{EFW}}$	$\delta t_{n_{EFW}}$
	[min]		[min]		[min]		[min]	
20020201 20:00/0203 04:00	0.97	3	1.00	12	0.96	3	0.98	3
20020211 13:00/0212 12:00	0.86	2	1.00	0	0.99	19	0.99	18
20020218 09:00/0219 02:00	0.95	1	1.00	-4	1.00	-3	0.97	-2
20020219 06:30/0219 15:00	0.96	1	0.99	-1	0.99	-60	1.00	60
20020220 18:30/0222 00:00	0.90	4	1.00	4	0.93	-20	0.98	3
20020318 17:30/0319 02:30	0.91	2	1.00	21	0.98	51	0.99	6
20020412 20:30/0413 02:00	0.91	5	0.99	-53	0.94	60	0.98	12
20021227 12:00/1228 03:00	0.84	4	1.00	-2	0.99	-21	0.99	22
20021229 20:00/1230 16:00	0.76	1	1.00	1	0.99	-30	0.98	43
20030106 06:00/0106 19:00	0.82	5	1.00	7	0.99	3	0.95	-60
20030108 07:00/0109 03:30	0.56	10	1.00	41	0.99	9	0.97	-56
20030113 08:30/0113 18:00	0.94	3	1.00	5	1.00	3	0.97	-1
20030120 07:30/0120 13:00	0.86	3	1.00	8	1.00	4	1.00	-55
20030122 12:00/0123 14:00	0.85	2	1.00	3	1.00	3	0.92	-60
20030124 18:00/0126 00:00	0.78	3	1.00	0	0.99	-60	0.99	60
20030127 16:00/0128 06:00	0.89	-1	1.00	-3	0.96	1	0.89	12
20030129 12:00/0130 18:00	0.92	2	1.00	4	0.95	-59	0.98	1

1025 **Table 1.** The studied solar wind intervals. The correlation coefficients (C_{B_z} , C_{V_x} , $C_{n_{CIS}}$,
1026 $C_{n_{EFW}}$) and time shift (δt_{V_x} , $\delta t_{n_{CIS}}$, $\delta t_{n_{EFW}}$) in minutes of the magnetic field GSE Z compo-
1027 nent (B_z), solar wind velocity X component (V_x), CIS and EFW densities (n_{CIS} , n_{EFW}).

Table 2: The studied magnetosheath intervals. The correlation coefficients (C_{B_z} , C_{V_x} , $C_{n_{CIS}}$, $C_{n_{EFW}}$) and time shift (δt_{V_x} , $\delta t_{n_{CIS}}$, $\delta t_{n_{EFW}}$) in minutes of the magnetic field GSE Z component (B_z), solar wind velocity X component (V_x), CIS and EFW densities (n_{CIS} , n_{EFW}). In the empty slots the correlation calculation gives invalid result.

Start/End	C_{B_z}	δt_{B_z}	C_{V_x}	δt_{V_x}	$C_{n_{CIS}}$	$\delta t_{n_{CIS}}$	$C_{n_{EFW}}$	$\delta t_{n_{EFW}}$
		[min]		[min]		[min]		[min]
20020201 13:30/0201 18:30	0.92	1	0.98	57	0.99	60	0.98	60
20020208 18:15/0209 00:00	0.78	3	0.95	60	0.98	-53	0.98	-54
20020211 02:30/0211 09:00	0.81	0	0.99	-21	1.00	0	0.99	0
20020212 16:30/0212 21:00	0.86	3	1.00	54	0.99	30	0.99	30
20020219 17:30/0219 23:00	0.78	4	0.99	37	1.00	6	1.00	6
20020222 23:00/0223 06:30	0.69	1	0.97	-60	0.99	-52	0.99	-48
20020227 16:30/0227 23:15	0.53	60	0.98	-31	1.00	-38	1.00	-11
20020310 18:30/0311 00:30	0.98	3	0.98	20	0.99	8	0.99	-2
20020311 14:00/0311 19:00	0.88	5	0.97	36	0.99	-3	0.99	-40
20020406 19:00/0407 01:15	0.79	1	0.97	-60	0.98	-56	0.98	-56
20020410 17:30/0410 23:00	0.89	5	0.99	-52	1.00	3	1.00	5
20020411 11:30/0411 16:30	0.84	3	0.99	40	0.99	3	0.99	3
20020418 18:30/0418 22:45	0.93	59	0.99	-60	0.99	60	0.98	60
20020421 04:30/0421 07:45	0.98	55	1.00	-60	1.00	-60	1.00	-60
20020422 11:45/0422 15:45	0.77	-5	0.98	-17	0.99	-15	0.99	-16
20020423 08:30/0423 12:30	0.94	31	1.00	4	0.99	16	1.00	16
20020430 12:30/0430 17:00	0.81	58	0.99	23	0.99	-18		
20020505 07:00/0505 11:15	0.83	59	0.99	32	0.99	-60		
20020506 19:15/0507 00:15	0.89	-28	0.99	-60	0.98	-36		
20020507 17:30/0507 23:00	0.94	1	0.99	47	0.99	-47		
20020514 22:45/0515 03:00	0.82	49	0.99	-60	0.99	32	0.99	-37
20020517 07:00/0517 12:15	0.76	-6	1.00	-5	0.99	-4	0.99	-3
20020518 13:30/0518 19:30	0.76	1	0.99	11	0.98	-2	0.98	-2

Continued on next page

Table 2 – *Continued from previous page*

Start/End	C_{B_z}	δt_{B_z}	C_{V_x}	δt_{V_x}	$C_{n_{CIS}}$	$\delta t_{n_{CIS}}$	$C_{n_{EFW}}$	$\delta t_{n_{EFW}}$
		[min]		[min]		[min]		[min]
20020519 20:00/0520 03:30	0.98	2	1.00	-9	0.99	-4	0.99	-50
20020520 10:45/0520 20:15	0.80	1	0.99	-3	0.95	-1	0.99	-1
20020522 02:00/0522 08:45	0.53	52	0.99	4	0.99	11	0.99	22
20020527 02:15/0527 17:15	0.80	-3	0.99	-2	0.98	0	0.99	0
20020530 05:00/0530 10:30	0.30	3	1.00	-23	0.99	4	0.99	3
20020601 19:30/0602 01:00	0.68	-2	1.00	17	0.99	-6	0.99	-7
20020602 21:45/0603 17:45	0.65	-5	0.99	0	0.98	3	0.99	3
20020605 10:30/0606 06:00	0.20	0	0.99	-7	0.98	10	0.98	9
20020607 18:00/0607 22:00	0.93	-35	1.00	-34	0.99	16	0.99	15
20020608 01:15/0608 18:15	0.54	-4	1.00	-39	0.97	-6	0.97	-6
20020610 01:30/0610 09:30	0.80	5	1.00	8	0.99	3	1.00	-7
20020610 11:00/0611 01:00	0.89	-4	1.00	-35	0.99	24	0.99	7
20020612 18:30/0613 06:15	0.45	-2	0.99	-7	0.97	-3	0.97	-33
20020615 07:00/0615 23:30			1.00	47	0.98	-3	0.98	-5
20020617 05:00/0618 03:45	0.79	3	1.00	28	0.98	9	0.99	8
20020620 04:00/0620 11:00	0.65	-8	0.99	-6	0.98	11	0.98	6
20020622 14:30/0622 18:00	0.99	56	1.00	33	1.00	16	1.00	16
20021201 04:15/1202 07:45	0.41	1	1.00	2	0.99	6	0.99	6
20021203 15:30/1204 19:30	0.72	1	0.99	60	0.98	59	0.98	59
20021207 00:30/1207 07:45	0.53	38	0.99	-50	0.99	-20	0.99	20
20021208 09:30/1209 08:00	0.72	3	0.99	-36	0.98	5	0.98	5
20021212 23:30/1213 14:30	0.53	5	1.00	36	0.99	-3	0.95	-56
20021213 21:15/1214 09:30	0.96	5	1.00	-35	0.99	-5	0.99	-46
20021215 12:45/1216 18:00	0.80	2	0.99	-60	0.95	-60	0.98	30
20021217 16:30/1218 01:45	0.91	2	1.00	-54	0.99	3	0.99	3
20021220 01:30/1220 06:15	0.93	0	1.00	60	0.99	2	0.99	3
20021223 02:15/1223 13:00	0.93	1	0.97	39	0.94	50	0.99	-14
20021223 14:00/1223 22:30	0.88	1	1.00	-2	0.99	-1	1.00	-3
20021224 19:00/1225 01:45	0.96	0	1.00	-43	0.99	12	0.99	28

Continued on next page

Table 2 – *Continued from previous page*

Start/End	C_{B_z}	δt_{B_z}	C_{V_x}	δt_{V_x}	$C_{n_{CIS}}$	$\delta t_{n_{CIS}}$	$C_{n_{EFW}}$	$\delta t_{n_{EFW}}$
		[min]		[min]		[min]		[min]
20021225 23:45/1226 07:15	0.97	7	1.00	-18	0.99	56	0.99	56
20021226 23:00/1227 09:45	0.83	2	1.00	2	0.99	4	0.99	2
20021229 11:45/1229 17:00	0.63	2	1.00	-32	0.99	49	0.99	48
20021230 17:45/1231 01:00	0.74	1	0.99	55	0.98	60	0.98	22
20021231 23:00/0101 05:15	0.92	2	1.00	0	0.99	-54	1.00	-56
20030105 14:00/0105 21:00	0.73	1	1.00	1	1.00	-60	0.99	-60
20030106 23:15/0107 03:00	0.70	4	0.99	41	1.00	56	1.00	-60
20030109 08:45/0109 16:15			0.91	-55	0.98	-13	0.98	-25
20030110 07:15/0110 15:15	0.95	1	0.99	-7	0.99	2	0.98	11
20030111 08:15/0111 22:30	0.88	1	0.99	-59	0.94	-15	0.94	8
20030112 17:30/0113 00:15	0.98	0	1.00	-47	0.99	39	0.99	51
20030114 00:30/0114 08:30	0.86	-1	0.99	-60	0.98	23	0.98	8
20030116 10:15/0116 17:45	0.64	60	0.93	52	0.99	60	0.99	30
20030117 09:30/0117 13:30	0.70	-3	1.00	7	1.00	-31	1.00	-33
20030118 23:30/0119 03:45	0.97	3	1.00	-12	1.00	7	0.99	7
20030119 21:00/0120 01:00	0.96	3	1.00	6	1.00	38	1.00	20
20030121 06:30/0121 11:30	0.87	-3	0.98	40	0.99	8	1.00	8
20030122 04:45/0122 09:30	0.76	-2	1.00	1	1.00	-7	1.00	-4
20030126 01:45/0126 06:30	0.90	3	0.99	-15	1.00	-51	0.99	24
20030127 08:15/0127 13:00	1.00	10	1.00	-60	0.99	-1	0.99	1
20030128 12:30/0128 17:15	0.77	60	0.99	-22	0.99	-5	0.99	21
20030130 19:45/0131 00:15	0.98	2	0.99	52	0.99	8	0.99	8

Table 3: The studied magnetosphere intervals (UT).

Start/End
20020213 23:00/0214 01:30
20020217 18:30/0218 02:00
20020220 00:45/0220 12:00
20020222 11:15/0222 20:15
20020225 02:15/0225 08:30
20020227 06:00/0227 12:00
20020302 00:00/0302 03:15
20020306 10:00/0306 18:30
20020308 17:30/0309 06:00
20020311 02:15/0311 12:00
20020313 11:15/0314 00:15
20020316 04:45/0316 08:00
20020318 09:00/0318 14:45
20020320 20:30/0320 23:55
20020323 04:00/0323 09:45
20020327 23:45/0328 06:15
20020330 07:15/0330 12:45
20020401 19:30/0401 22:00
20020406 09:30/0406 18:00
20020408 15:00/0409 00:00
20020410 23:30/0411 09:45
20020413 08:30/0413 19:00
20020416 18:00/0417 04:30
20020418 06:00/0418 12:00
20020420 15:00/0420 23:00
20020422 20:00/0423 07:00
20020425 08:30/0425 18:00
20020430 04:40/0430 12:00
20020504 14:30/0504 16:45

Continued on next page

Table 3 – *Continued from previous page*

Start/End
20020505 02:30/0505 07:00
20020507 01:30/0507 15:45
20020508 11:00/0510 04:15
20020512 02:45/0512 09:30
20020514 10:30/0514 12:45
20020519 00:30/0519 19:30
20020521 01:30/0521 22:00
20020523 23:30/0524 02:00
20020524 19:00/0525 08:15
20020526 07:30/0526 10:30
20020528 20:00/0529 05:00
20020531 02:15/0531 13:30
20020602 04:30/0602 07:30
20020602 12:00/0602 21:30
20020604 08:30/0605 07:00
20020606 14:30/0607 16:30
20020609 06:00/0609 20:00
20020611 11:00/0612 13:00
20020614 01:00/0614 16:00
20020616 08:00/0616 18:00
20020620 13:30/0622 01:00
20020623 13:00/0623 17:00
20020624 04:00/0624 10:15
20020630 17:45/0701 15:00
20020701 21:00/0703 10:30
20020703 23:00/0706 03:15
20020707 01:00/0708 23:00
20020710 11:30/0714 03:30
20020714 15:45/0715 15:30
20020716 23:30/0717 16:00

Continued on next page

Table 3 – *Continued from previous page*

Start/End
20020718 05:45/0722 11:00
20020722 23:45/0728 01:00
20020728 02:00/0804 03:45
20020804 04:45/0811 06:15
20020811 07:30/0816 01:00
20020816 15:30/0818 09:00
20020818 10:00/0825 11:30
20020825 13:00/0901 14:15
20020901 17:15/0903 23:30
20020905 02:15/0906 16:30
20020907 10:30/0908 17:00
20020908 18:00/0915 19:30
20020915 21:00/0922 22:30
20020923 00:00/0923 23:30
20020924 03:30/0928 22:45
20020928 23:30/0930 01:00
20020930 02:15/1006 17:00
20021006 17:45/1007 03:30
20021007 05:00/1007 17:30
20021008 07:30/1010 22:00
20021010 22:30/1012 22:30
20021012 23:00/1014 06:30
20021014 09:00/1016 04:00
20021016 14:00/1019 00:15
20021019 01:30/1019 22:00
20021021 04:00/1022 19:30
20021022 22:30/1026 02:30
20021026 04:00/1029 20:15
20021030 01:30/1102 08:00
20021102 22:00/1104 22:00

Continued on next page

Table 3 – *Continued from previous page*

Start/End
20021106 00:00/1107 18:00
20021108 02:00/1109 18:45
20021111 00:00/1112 01:30
20021113 03:45/1114 14:15
20021115 20:30/1116 23:00
20021118 01:00/1118 23:30
20021120 17:00/1121 06:00
20021122 21:30/1124 01:00
20021125 04:00/1126 08:30
20021127 20:00/1128 18:30
20021130 04:00/1201 01:30
20021202 14:30/1203 09:00
20021204 22:00/1205 19:30
20021207 09:00/1207 16:30
20021207 18:00/1207 22:00
20021209 16:30/1210 14:30
20021212 13:45/1212 21:30
20021214 13:30/1214 20:00
20021214 21:00/1215 07:30
20021216 21:00/1217 15:00
20021219 08:00/1219 19:30
20021221 15:45/1221 23:15
20021222 00:30/1222 08:45
20021224 02:30/1224 14:00
20021226 10:00/1226 19:00
20021228 19:30/1229 02:30
20021229 04:00/1229 10:00
20021231 05:00/1231 18:45
20030102 12:30/0102 20:45
20030104 20:45/0105 06:00

Continued on next page

Table 3 – *Continued from previous page*

Start/End
20030105 07:00/0105 13:30
20030107 05:45/0107 21:00
20030109 17:00/0110 00:45
20030112 00:00/0112 09:15
20030112 10:30/0112 16:00
20030114 11:00/0114 20:00
20030116 20:30/0116 22:45
20030119 04:30/0119 09:30
20030119 14:00/0119 17:00
20030121 13:30/0121 21:30
20030126 07:30/0126 15:45
20030128 17:45/0129 08:15
20030131 01:30/0131 11:45

Start/End	OMNI			Cluster SC3			
	B_z [nT]	V_x [km/s]	P [cm $^{-3}$]	B_z	V_x	n_{CIS}	n_{EFW}
20020201 20:00/0203 04:00	-1.25	-373.52	4.08	y	y	n	y
20020211 13:00/0212 12:00	0.03	-533.11	2.18	y	y	y	y
20020218 09:00/0219 02:00	2.56	-362.41	3.46	y	n	n	y
20020219 06:30/0219 15:00	3.55	-401.63	1.25	y	y	n	n
20020220 18:30/0222 00:00	1.95	-440.18	1.96	y	y	n	y
20020318 17:30/0319 02:30	3.79	-429.30	15.34	y	n	n	n
20020412 20:30/0413 02:00	-1.81	-420.35	3.24	y	n	n	y
20021227 12:00/1228 03:00	0.09	-714.40	2.72	y	n	n	y
20021229 20:00/1230 16:00	-0.37	-526.40	2.26	y	y	n	n
20030106 06:00/0106 19:00	2.25	-399.91	1.50	y	n	n	n
20030108 07:00/0109 03:30	-0.58	-280.80	2.97	n	n	y	n
20030113 08:30/0113 18:00	0.68	-397.83	1.72	y	y	y	n
20030120 07:30/0120 13:00	2.16	-630.69	2.43	y	y	y	y
20030122 12:00/0123 14:00	0.13	-608.96	3.41	y	y	y	n
20030124 18:00/0126 00:00	-0.71	-739.68	2.87	y	y	n	n
20030127 16:00/0128 06:00	-0.92	-451.84	3.12	y	y	n	n
20030129 12:00/0130 18:00	-3.09	-450.00	3.96	y	y	n	y

1030 **Table 4.** The average OMNI input parameters in the solar wind and the good/bad agreement
 1031 of the GUMICS-4 simulations to the Cluster B_z magnetic field component, the V_x solar wind
 1032 speed component, the n_{CIS} solar wind density measured by the Cluster CIS HIA instrument and
 1033 the n_{EFW} solar wind density calculated from the spacecraft potential measured by the Cluster
 1034 EFW instrument in the solar wind.

Table 5: The average OMNI input parameters in the solar wind and the good/bad agreement of the GUMICS–4 simulations to the Cluster B_z magnetic field component, the V_x solar wind speed component, the n_{CIS} solar wind density measured by the Cluster CIS HIA instrument and the n_{EFW} solar wind density calculated from the spacecraft potential measured by the Cluster EFW instrument in the magnetosheath.

Start/End	OMNI			Cluster SC3			
	B_z	V_x	P	B_z	V_x	n_{CIS}	n_{EFW}
	[nT]	[km/s]	[cm $^{-3}$]				
20020201 13:30/0201 18:30	0.19	-342.87	4.62	y	n	n	n
20020208 18:15/0209 00:00	-0.48	-508.16	1.61	y	n	n	n
20020211 02:30/0211 09:00	-1.85	-425.67	1.78	y	y	y	y
20020212 16:30/0212 21:00	2.98	-509.22	2.34	y	n	n	n
20020219 17:30/0219 23:00	1.46	-431.50	1.46	y	y	y	y
20020222 23:00/0223 06:30	0.86	-391.22	1.14	y	n	n	n
20020227 16:30/0227 23:15	1.89	-343.13	1.52	n	n	n	n
20020310 18:30/0311 00:30	-2.81	-379.46	1.78	y	y	y	y
20020311 14:00/0311 19:00	1.63	-371.43	2.68	n	n	n	n
20020406 19:00/0407 01:15	-2.71	-333.13	0.93	y	n	n	n
20020410 17:30/0410 23:00	0.31	-312.43	4.42	n	n	y	y
20020411 11:30/0411 16:30	-1.50	-494.02	4.25	y	y	n	n
20020418 18:30/0418 22:45	-0.92	-450.82	0.30	n	n	n	n
20020421 04:30/0421 07:45	0.40	-455.69	1.37	n	n	n	n
20020422 11:45/0422 15:45	0.25	-419.98	1.14	n	n	y	y
20020423 08:30/0423 12:30	2.77	-507.99	6.82	n	n	n	n
20020430 12:30/0430 17:00	2.15	-479.51	3.02	n	n	n	n
20020505 07:00/0505 11:15	0.20	-336.81	1.74	n	n	n	n
20020506 19:15/0507 00:15	0.78	-390.00	2.46	y	n	n	n
20020507 17:30/0507 23:00	2.87	-392.40	3.49	y	n	n	n
20020514 22:45/0515 03:00	-2.42	-414.01	1.82	n	n	n	n

Continued on next page

Table 5 – *Continued from previous page*

Start/End	OMNI			Cluster SC3			
	B_z [nT]	V_x [km/s]	P $[cm^{-3}]$	B_z	V_x	n_{CIS}	n_{EFW}
20020517 07:00/0517 12:15	-0.39	-379.32	1.52	y	y	y	y
20020518 13:30/0518 19:30	0.63	-345.87	1.59	n	n	y	y
20020519 20:00/0520 03:30	4.75	-408.56	1.12	y	y	y	y
20020520 10:45/0520 20:15	0.74	-448.89	1.93	y	y	y	y
20020522 02:00/0522 08:45	-1.07	-398.12	1.63	n	y	y	y
20020527 02:15/0527 17:15	-3.11	-542.53	2.07	y	y	y	y
20020530 05:00/0530 10:30	0.03	-493.86	2.08	y	n	y	y
20020601 19:30/0602 01:00	-3.38	-342.27	4.16	y	y	y	y
20020602 21:45/0603 17:45	0.38	-435.47	1.89	y	y	y	y
20020605 10:30/0606 06:00	-0.42	-394.49	1.08	y	y	n	n
20020607 18:00/0607 22:00	-1.60	-291.85	1.80	y	y	y	y
20020608 01:15/0608 18:15	0.06	-335.39	2.74	y	n	y	y
20020610 01:30/0610 09:30	1.60	-465.52	3.00	y	y	y	y
20020610 11:00/0611 01:00	-2.27	-419.86	2.16	y	n	y	y
20020612 18:30/0613 06:15	-1.13	-351.03	1.16	y	y	y	y
20020615 07:00/0615 23:30	-1.16	-334.27	2.84	n	n	y	y
20020617 05:00/0618 03:45	0.78	-351.47	1.87	y	n	y	y
20020620 04:00/0620 11:00	0.46	-485.48	1.73	y	y	y	y
20020622 14:30/0622 18:00	-0.72	-429.02	1.93	n	n	y	y
20021201 04:15/1202 07:45	-1.09	-499.23	2.62	y	y	y	y
20021203 15:30/1204 19:30	0.34	-449.09	2.06	y	n	n	n
20021207 00:30/1207 07:45	0.80	-451.80	7.33	n	n	y	y
20021208 09:30/1209 08:00	0.60	-600.27	1.49	y	n	y	y
20021212 23:30/1213 14:30	0.10	-337.77	1.32	y	n	n	n
20021213 21:15/1214 09:30	-0.74	-361.19	2.99	y	n	y	y
20021215 12:45/1216 18:00	1.32	-479.48	1.53	y	n	n	n
20021217 16:30/1218 01:45	4.56	-393.99	2.49	y	n	y	y
20021220 01:30/1220 06:15	-1.21	-530.62	3.01	y	n	y	y

Continued on next page

Table 5 – *Continued from previous page*

Start/End	OMNI			Cluster SC3			
	B_z [nT]	V_x [km/s]	P $[cm^{-3}]$	B_z	V_x	n_{CIS}	n_{EFW}
20021223 02:15/1223 13:00	-2.32	-516.12	2.22	y	n	n	n
20021223 14:00/1223 22:30	0.89	-519.77	2.55	y	y	y	y
20021224 19:00/1225 01:45	0.88	-523.86	3.41	y	n	y	y
20021225 23:45/1226 07:15	-0.61	-414.38	2.21	y	y	n	n
20021226 23:00/1227 09:45	-1.79	-618.14	6.20	y	y	y	y
20021229 11:45/1229 17:00	-0.41	-580.12	2.39	y	n	n	n
20021230 17:45/1231 01:00	-1.01	-483.60	1.93	y	n	n	y
20021231 23:00/0101 05:15	0.60	-418.95	1.94	y	n	n	n
20030105 14:00/0105 21:00	-0.03	-414.46	1.69	y	n	n	n
20030106 23:15/0107 03:00	-1.62	-392.29	1.56	n	n	n	n
20030109 08:45/0109 16:15	1.45	-272.82	2.31	n	n	n	n
20030110 07:15/0110 15:15	-2.11	-401.03	2.72	y	n	y	y
20030111 08:15/0111 22:30	-0.20	-433.33	1.24	y	n	n	y
20030112 17:30/0113 00:15	1.53	-389.62	1.45	y	n	n	n
20030114 00:30/0114 08:30	-1.67	-388.53	2.27	y	n	n	y
20030116 10:15/0116 17:45	-1.20	-328.91	1.22	n	n	n	n
20030117 09:30/0117 13:30	-1.36	-327.09	2.55	y	y	y	y
20030118 23:30/0119 03:45	6.41	-459.46	4.82	y	y	y	y
20030119 21:00/0120 01:00	1.52	-597.95	2.38	y	n	y	y
20030121 06:30/0121 11:30	-1.77	-670.25	1.50	y	n	n	n
20030122 04:45/0122 09:30	0.11	-588.87	2.30	y	n	y	y
20030126 01:45/0126 06:30	-0.24	-713.82	2.75	y	y	y	y
20030127 08:15/0127 13:00	7.94	-509.30	0.47	y	n	y	y
20030128 12:30/0128 17:15	4.95	-443.83	4.15	y	y	y	y
20030130 19:45/0131 00:15	4.21	-510.33	2.63	y	n	y	y

Table 6: Intervals around the studied bow shock crossings. The Cluster SC3 crossed the bow shock in all cases. The 2nd column shows whether the bow shock is visible in the GUMICS–4 simulations.

Start/End	GUMICS Bow Shock
20020201 12:00/0202 00:00	+
20020203 00:00/0203 12:00	+
20020206 06:00/0206 18:00	+
20020208 18:00/0209 06:00	+
20020211 06:00/0211 18:00	+
20020212 12:00/0212 18:00	+
20020213 12:00/0213 18:00	+
20020216 00:00/0216 12:00	+
20020217 06:00/0217 12:00	-
20020218 06:00/0218 18:00	+
20020219 00:00/0219 18:00	+
20020220 12:00/0221 00:00	+
20020221 18:00/0222 00:00	+
20020301 06:00/0301 12:00	+
20020304 12:00/0304 18:00	+
20020306 00:00/0306 06:00	+
20020307 00:00/0307 06:00	+
20020308 06:00/0308 12:00	+
20020309 06:00/0309 12:00	+
20020310 12:00/0311 00:00	+
20020311 18:00/0312 00:00	+
20020313 00:00/0313 06:00	-
20020314 00:00/0314 12:00	+
20020316 06:00/0316 18:00	+
20020318 12:00/0319 00:00	+
20020323 12:00/0323 18:00	+

Continued on next page

Table 6 – *Continued from previous page*

Start/End	GUMICS Bow Shock
20020325 18:00/0326 06:00	–
20020327 06:00/0327 12:00	+
20020329 18:00/0330 00:00	–
20020402 00:00/0402 06:00	+
20020405 18:00/0406 00:00	–
20020407 00:00/0407 06:00	–
20020409 06:00/0409 12:00	–
20020410 12:00/0410 18:00	–
20020411 12:00/0411 18:00	–
20020413 00:00/0413 06:00	+
20020413 18:00/0414 06:00	+
20020420 00:00/0420 06:00	+
20020423 12:00/0423 23:00	+
20020427 00:00/0427 06:00	+
20020428 06:00/0428 12:00	+
20020430 18:00/0501 00:00	+
20020505 06:00/0505 18:00	–
20020507 18:00/0509 06:00	+
20020510 06:00/0510 12:00	+
20020513 12:00/0513 18:00	+
20020515 00:00/0515 06:00	–
20020520 00:00/0520 06:00	+
20020522 06:00/0522 12:00	+
20020522 18:00/0523 06:00	+
20021206 06:00/1207 06:00	+
20021218 00:00/1219 00:00	+
20021220 18:00/1221 00:00	+
20021221 00:00/1221 12:00	+
20021222 12:00/1223 00:00	+
20021223 00:00/1223 06:00	+

Continued on next page

Table 6 – *Continued from previous page*

Start/End	GUMICS Bow Shock
20021225 06:00/1226 00:00	+
20021227 06:00/1228 00:00	+
20021228 00:00/1228 12:00	+
20021229 12:00/1230 00:00	+
20030101 06:00/0102 00:00	+
20030103 06:00/0103 12:00	+
20030104 00:00/0104 18:00	+
20030106 00:00/0107 00:00	+
20030108 00:00/0108 12:00	+
20030113 00:00/0114 06:00	+
20030115 00:00/0115 12:00	+
20030118 18:00/0119 00:00	+
20030120 00:00/0121 12:00	+
20030122 06:00/0122 12:00	+
20030123 12:00/0124 00:00	+
20030124 12:00/0124 18:00	+
20030126 00:00/0126 06:00	+
20030127 00:00/0127 18:00	+
20030128 06:00/0128 18:00	+
20030129 06:00/0129 12:00	+
20030130 18:00/0131 00:00	+

Table 7: Intervals around the studied magnetopause crossings.
The Cluster SC3 crossed the magnetopause in all cases. The
2nd column shows whether the magnetopause is visible in the
GUMICS–4 simulations.

Start/End	GUMICS Magnetopause
20020203 06:00/0203 12:00	+
20020206 06:00/0206 12:00	-
20020211 00:00/0211 06:00	+
20020218 00:00/0218 06:00	+
20020225 06:00/0225 12:00	+
20020302 00:00/0302 06:00	+
20020306 18:00/0307 00:00	-
20020308 12:00/0308 18:00	-
20020311 12:00/0311 18:00	+
20020313 18:00/0314 00:00	-
20020314 00:00/0314 06:00	+
20020323 06:00/0323 12:00	+
20020330 12:00/0330 18:00	-
20020404 06:00/0404 12:00	-
20020409 00:00/0409 06:00	-
20020418 12:00/0418 18:00	+
20020422 12:00/0422 18:00	-
20020429 18:00/0430 00:00	-
20020507 12:00/0507 18:00	-
20020509 06:00/0509 12:00	-
20020510 00:00/0510 06:00	-
20020514 18:00/0515 00:00	-
20020519 12:00/0519 18:00	-
20020520 12:00/0521 00:00	-
20020522 00:00/0522 06:00	-
20020529 00:00/0529 12:00	-

Continued on next page

Table 7 – *Continued from previous page*

Start/End	GUMICS Magnetopause
20020530 06:00/0530 18:00	–
20020531 18:00/0601 00:00	–
20020602 18:00/0603 00:00	–
20020604 06:00/0604 12:00	–
20020605 06:00/0606 18:00	–
20020607 12:00/0608 06:00	+
20020609 00:00/0609 06:00	–
20020610 00:00/0610 06:00	–
20020611 00:00/0611 12:00	–
20020612 06:00/0614 00:00	–
20020614 18:00/0615 06:00	–
20020616 00:00/0616 12:00	+
20020620 00:00/0620 18:00	–
20020622 06:00/0622 18:00	–
20020704 12:00/0705 00:00	–
20020706 00:00/0706 12:00	+
20020709 00:00/0709 18:00	–
20020715 18:00/0716 12:00	–
20030105 06:00/0105 18:00	+
20030110 00:00/0110 12:00	+
20030112 12:00/0112 18:00	–
20030117 06:00/0117 12:00	+
20030121 06:00/0121 12:00	+
20030122 00:00/0122 06:00	–
20030126 18:00/0127 00:00	+
20030128 12:00/0128 18:00	+
20030129 00:00/0129 12:00	+
20030131 12:00/0201 00:00	+

Start/End	GUMICS Neutral Sheet
20020901 19:00/0902 00:00	–
20020906 14:00/0906 16:30	+
20020913 17:30/0913 20:00	+
20020918 13:00/0918 14:30	–
20020920 20:30/0921 02:00	+
20020928 03:00/0928 07:00	+
20021002 16:00/1003 00:00	–
20021014 12:30/1014 23:00	+
20021017 03:00/1017 04:00	–

¹⁰³⁸ **Table 8.** Intervals around the studied neutral sheet crossings in the tail. The Cluster SC3
¹⁰³⁹ crossed the neutral sheet in all cases. The 2nd column shows whether the neutral sheet is visible
¹⁰⁴⁰ in the GUMICS–4 simulations.